Journal of Computational Physics 229 (2010) 3916–3937

Contents lists available at ScienceDirect

Journal of Computational Physics

journal homepage: www.elsevier.com/locate/jcp

A hybrid scheme for gas–dust systems stiffly coupled via viscous drag

Francesco Miniati *

Physics Department, Wolfgang-Pauli-Strasse 27, ETH Zürich, CH-8093 Zürich, Switzerland

ARTICLE INFO

Article history:
Received 31 August 2009
Received in revised form 20 January 2010
Accepted 26 January 2010
Available online 1 February 2010

Keywords:
Godunov methods
Particle-in-cell methods
Stiff equations

ABSTRACT

We present a stable and convergent method for studying a system of gas and dust, coupled through viscous drag in both non-stiff and stiff regimes. To account for the effects of dust drag in the update of the fluid quantities, we employ a fluid description of the dust component and study the modified gas-dust hyperbolic system following the approach in Miniati and Colella [19]. In addition to two entropy waves for the gas and dust components, respectively, the extended system includes three waves driven partially by gas pressure and partially by dust drift, which, in the limit of vanishing coupling, tend to the two original acoustic waves and the unhindered dust streaming. Based on this analysis we formulate a predictor step providing first order accurate reconstruction of the time-averaged state variables at cell interfaces, whence a second order accurate estimate of the conservative fluxes can be obtained through a suitable linearized Riemann solver. The final source term update is carried out using a one-step, second order accurate, L-stable, predictor corrector asymptotic method (the α-QSS method suggested by Mott et al. [21]). This procedure completely defines a two-fluid method for gas-dust system. Using the updated fluid solution allows us to then advance the individual particle solutions, including self-consistently the time evolution of the gas velocity in the estimate of the drag force. This is done with a suitable particle scheme also based on the α-QSS method. A set of benchmark problems shows that our method is stable and convergent. When dust is modeled as a fluid (two-fluid) second order accuracy is achieved in both stiff and non-stiff regimes, whereas when dust is modeled with particles (hybrid) second order is achieved in the non-stiff regime and first order otherwise.

1. Introduction

We wish to solve the system of partial differential equations describing two systems coupled through the exchange of momentum through a viscous term proportional to their relative velocity. This situation characterizes a variety of problems, among others gas–dust coupling in protoplanetary disks, the motion of polymer molecules in biological fluids [26], drift of different ion species in the planetary plasma [5]. We are interested in addressing the case in which the viscous coupling becomes stiff, such that the relaxation time characterizing it is significantly shorter than the smallest timescale characterizing the fluid system, typically defined as sound crossing time of a resolution element. Although the results presented in this paper can possibly be extended to other physical systems as those mentioned above, in the following we specialized our analysis to the case of a gaseous and a dust component, coupled through a drag term as well as gravity, typical of a protoplanetary disk.

* Tel.: +41 0 44 633 6495; fax: +41 0 44 633 1238.
E-mail address: fm@phys.ethz.ch

0021-9991/$ - see front matter © 2010 Elsevier Inc. All rights reserved.
doi:10.1016/j.jcp.2010.01.034

Without loss of generality we start considering the problem in one dimension. The gas component is described by the equations of hydrodynamics with a suitable source term, namely

$$\frac{\partial U}{\partial t}+\frac{\partial F(U)}{\partial x}=S(U), \tag{1}$$

where

$$U=\begin{pmatrix}\rho_g\\ \rho_g u_g\\ \rho_g E\end{pmatrix},\quad F(U)=\begin{pmatrix}\rho_g u_g\\ \rho_g u_g^2+P\\ u_g\,[\rho E+P]\end{pmatrix},\quad S(U)=\begin{pmatrix}0\\ \rho_g(f_d-\nabla\phi)\\ u_g\rho_g(f_d-\nabla\phi)\end{pmatrix}. \tag{2}$$

The fluid quantities (with subscript g for gas) have their usual meaning, whereas f_d and $-\nabla\phi$ describe drag and gravitational acceleration, respectively, which will be specified below. The dust particles move along the following trajectories in phase-space

$$\frac{dx_d}{dt}=v_d, \tag{3}$$

$$\frac{dv_d}{dt}=-\kappa_d\,(v_d-u_g)-\nabla\phi, \tag{4}$$

where, x_d and v_d are the dust particles position and velocity, respectively. We consider particles sizes that are small compared to the gas particle mean free path (Epstein's regime) so that the drag coefficient is

$$\kappa_d=\kappa_0\rho_g c,\quad \kappa_0\equiv\frac{1}{\hat{\rho}_d s}. \tag{5}$$

Here, $\hat{\rho}_d$ and s indicate the dust grain's mass density and size, respectively, and c is the gas speed of sound. As shown below (Section 3.1), the back-reaction exerted by the dust particles on the gas in Eq. (2), takes the form

$$f_d=-\kappa_g(u_g-u_d),\quad \kappa_g=\kappa_0\rho_d c, \tag{6}$$

where u_d is the average dust velocity in the neighborhood of the considered fluid element, also to be defined below. Eqs. (5) and (6) indicate that the dust-gas coupling coefficients become very large in the limit of either/both small grain sizes or/and large dust density. In this case the relaxation between gas and dust is fast compared to the sound crossing time, which leads to numerically stiff conditions. In addition, in the case of large dust densities, the dust back-reaction on the gas dynamics is considerable and needs to be accounted for accurately.

In addition to the stiff conditions mentioned above, the problem is complicated by the fact that on the one hand the dust particles are collisionless and therefore best described with a particle method in phase-space. However, in the stiff regime, the particles effectively interact on a short timescale not only with the surrounding gas but also with the surrounding particles. Taking into account such interactions using directly a particle description complicates considerably the problem, to a level that in fact is not tractable.

In this paper, we formulate an algorithm to address such a problem. In particular, for the purpose of modeling efficiently the effects of the drag force by the dust particles on the fluid, we first obtain fluid description of the dust particle component, using a particle–mesh method. We then define an extended conservative system that includes both the gas and dust variables. This systems is advanced one time-step following a method which is an extension of the one described in Miniati and Colella [19]. More specifically, we use the fluid description of the dust to account for the modifications of the drag terms on the hyperbolic structure of the gas equations. This allows us to formulate a predictor step that gives first order accurate reconstruction of the time-averaged state variables at cell interfaces, whence a second order accurate estimates of the conservative fluxes can be obtained. With the dust component still described as a fluid, and a second order estimate of the fluxes for our extended conservative system, the source update is finally carried out using a one-step, second order accurate, predictor corrector asymptotic method as suggested by Mott et al. [21]. At the end of this procedure we have obtained a fluid solution that includes self-consistently the collective effect of the particles drag on the fluid.

We can then update the individual particle solutions using a suitable particle scheme that follows the particles along their characteristic trajectories in phase-space, taking into account the effect of drag from the fluid. The above knowledge of the fluid solution at the current and next time-step is crucial, however, to include self-consistently the time evolution of the gas velocity in the estimate of the drag force.

Finally, dust and gas are also coupled through gravity. However, this can be achieved in the standard way (e.g. [19]), namely by applying to both dust and gas components the gradient of their cumulative potential, ϕ, defined by the following Poisson's equation

$$\nabla^2\phi=-4\pi\mathcal{G}(\rho_g+\rho_d). \tag{7}$$

Several codes have already been published in the literature in order to study the coupled dust–gas–dynamics in protoplanetary disks. Among others, numerical codes based on the smoothed particle hydrodynamics method (SPH) approach have been developed for multifluid system [20,3,16], in addition to the simpler case in which dust is treated as a test particle and backreaction is neglected [24]. Grid based two-fluid methods have been around for a long time [8]. More recently they

have been extended to the MHD case [11], and to one-fluid models in which dust and gas are perfectly coupled [2]. Grid based hybrid (fluid + particles) methods have also been developed, including higher oder (sixth) spectral methods [14] and higher order (second) Godunov's method [1]. The novelty of our method consists in its ability to handle a variety of numerically stiff conditions both in the two-fluid and hybrid approaches. This is relevant because in a realistic setting stiff conditions arise in limited regions of a system and at a certain point in time during its evolution.

This paper is organized as follows. In Section 2. the particle integration scheme is presented. In Section 3 we describe the two-fluid approach that allows us to update the fluid solution one time step. This section, therefore includes a description of the methods for the fluid treatment of the dust component, the details of the semi-implicit predictor–corrector used for the source update. In Section 4 we present the Godunov predictor step, derive the characteristic analysis and provide a linearized Riemann solver, for the extended gas–dust fluid system. The stability of the method is addressed in Section 5. Accuracy and convergence tests are presented in Section 6 and a summary with discussion in Section 7 concludes the paper.

2. Particle integration scheme

The particle positions and velocities is updated with a predictor corrector method based on a variant of the Quasi-Steady-State method proposed by Mott et al. (the so called α-QSS [21]). Because we use this scheme extensively in this paper, we first describe it briefly in the following.

Consider the first order ordinary differential equation (ODE)

$$\frac{dy}{dt} = -p(t,y)y + q(t,y), \tag{8}$$

$$y(t_0) = y_0, \tag{9}$$

with $y \in \mathbb{R}, p, q : \mathbb{R} \times \mathbb{R} \to \mathbb{R}$.

If p and q are constants, the above system has the following exact solution given by Duhamel's formula,

$$y(t) = y_0 e^{-pt} + \frac{q}{p}(1 - e^{-pt}). \tag{10}$$

QSS methods are based on the asymptotic behavior of the above solution. When p and q depend on (y,t), a first order algorithm can be obtained by setting $p = p_0 \equiv p(t_0), q = q_0 \equiv q(t_0)$. This approach corresponds to the simplest QSS method and can be used to develop higher order methods by incorporating to some degree the time dependence of p, q into the solution. All QSS methods, however, reproduce the exact solution as p, q become constant. There are several QSS derived methods in the literature (cf. [23] for a review). Here we shall adopt the α-QSS method of Mott et al. [21]. This is a single-step, second order accurate, A-stable predictor–corrector method that can be summarized with the following procedure:

$$\tilde{y}(t_0 + \Delta t) = y_0 + \Delta t \frac{q_0 - p_0 y_0}{1 + \alpha(p_0 \Delta t) p_0 \Delta t}, \tag{11}$$

$$y(t_0 + \Delta t) = y_0 + \Delta t \frac{q_* - \bar{p} y_0}{1 + \alpha(\bar{p}\Delta t)\bar{p}\Delta t}, \tag{12}$$

$$q_* = q_0 + \alpha(\bar{p}\Delta t)[q(\tilde{y}, t_0 + \Delta t) - q_0], \tag{13}$$

$$\alpha(x) = \frac{1 - \frac{1-e^{-x}}{x}}{1 - e^{-x}}, \quad \bar{p} = \frac{p_0 + p(\tilde{y}, t_0 + \Delta t)}{2}. \tag{14}$$

Eqs. (11) and (12) correspond to the predictor and corrector step respectively. In addition to the case where p, q are constants, the above algorithm also returns the exact solution when p is constant and q is linear in time or p is linear in time and $q = 0$ [21].

In the following we derive a predictor–corrector algorithm based on Eqs. 11 and 12 to integrate the equation of motion of the dust particles given by (3) and (4). In the absence of drag it effectively reduces to a kick–drift–kick variant of the leapfrog scheme. For its derivation we assume that the gas velocity solution, v_g, has already been computed by the fluid scheme described below, at both t^n and $t^{n+1} = t^n + \Delta t$. The drag coefficient in (4) is a function of the gas density and sound speed and is interpolated at the particle position with a particle–mesh method, i.e.

$$\kappa_d(\mathbf{x_p}) = \sum_p w[x_p - x(\mathbf{i})]\kappa_d(\mathbf{i}), \tag{15}$$

where $w(s)$ is a weight function, $x(\mathbf{i})$, is the $\mathbf{i}$-th cell's center, and the summation is carried out over all cells. The velocity of the gas entering Eq. (4) must also be obtained by way of interpolation. By using the following expression

$$v_g(\mathbf{x_p}) = \frac{1}{\kappa_d(\mathbf{x_p})} \sum_p w[x_p - x(\mathbf{i})]\kappa_d(\mathbf{i}) u_g(\mathbf{i}), \tag{16}$$

total dust + gas momentum is conserved by construction in the non-stiff limit, and simple tests show that it is also conserved with high accuracy in the stiff regime.

We now present the algorithm, but a more detailed description of its derivation is provided in Appendix A. We first predict the particle position at t^{n+1} as

$$\tilde{x}_d = x_d^n + \beta(\kappa_d^n \Delta t)\, v_d^n \Delta t + [1 - \beta(\kappa_d^n \Delta t)]\, v_g^n \Delta t + \frac{1}{2}\nabla\phi^n \Delta t^2, \tag{17}$$

where $\beta(x) = \frac{1-e^{-x}}{x}$. As the particle travels from x_d^n to $\tilde{x}_d$ the gas velocity changes from $v_g^n = v_g(x_d^n)$ to $v_g^{n+1} = v_g(\tilde{x}_d)$. Since the above change is partially due to drag relaxation and partially due to the motion of the particles across a velocity gradient, we assume that the velocity experienced by the particle evolves as follows:

$$v_g(t) = v_g^n + \Delta v_g \left(e^{-\kappa_g \Delta t} \frac{t}{\Delta t} + 1 - e^{-\kappa_g t} \right), \tag{18}$$

where, $\Delta v_g \equiv v_g^{n+1} - v_g^n$. The above expression allows for a relaxation of the gas velocity towards the value v_g^{n+1} much faster then linear, which is important in the stiff case ($\kappa_g \Delta t \gg 1$). For the stiff case, this introduces some differences in our integration scheme with respect to the pure α-QSS method.

With the assumption of Eq. (18) we can carry out the time integration of the equation of motions for the particle velocity and position. In doing so, as in the α-QSS approach, we replace the time dependent drag coefficients with their time averages, that is the average between the values at position x_d^n and $\tilde{x}_d$, $\kappa_s \to \bar{\kappa}_s = \left[\kappa_s(x_d^n) + \kappa_s(\tilde{x}_d)\right]/2, s = d, g$. We thus obtain

$$\begin{aligned} x_d^{n+1} &= x_d^n + v_d^n \Delta t + [1 - \beta(\bar{\kappa}_d \Delta t)] \left(v_g^n - v_d^n \right) \Delta t + \nabla\phi^n \frac{\Delta t^2}{2} \\ &\quad + \Delta v_g \left\{ e^{-\bar{\kappa}_g \Delta t} \left[\frac{1}{2} - \frac{1 - \beta(\bar{\kappa}_d \Delta t)}{\bar{\kappa}_d \Delta t} \right] + 1 - \frac{\bar{\kappa}_d \beta(\bar{\kappa}_g \Delta t) - \bar{\kappa}_g \beta(\bar{\kappa}_d \Delta t)}{\bar{\kappa}_d - \bar{\kappa}_g} \right\} \Delta t, \end{aligned} \tag{19}$$

$$v_d^{n+1} = v_d^n + \beta(\bar{\kappa}_d \Delta t) \bar{\kappa}_d \left(v_g^n - v_d^n \right) \Delta t + \Delta v_g \left\{ e^{-\bar{\kappa}_g \Delta t} [1 - \beta(\bar{\kappa}_d)] + \frac{\bar{\kappa}_d \bar{\kappa}_g}{\bar{\kappa}_d - \bar{\kappa}_g} [\beta(\bar{\kappa}_g \Delta t) - \beta(\bar{\kappa}_d \Delta t)] \Delta t \right\}. \tag{20}$$

Remarkably the above particle method contains no explicit term arising from the stiff coupling of the particle component. Of course, the β terms take into account that the gas–dust coupling is fast compared to the time-step Δt. However, each particle motion is integrated individually though it effectively depends on the other particles solutions, and the scheme is essentially explicit in time, as it only involves the particle solution at time $t = n\Delta t$. Still the scheme is stable and convergent, and this is due to the fact that the gas velocity solution at times t and $t + \Delta t$, with which the particles interact, already contains the effect of the dust component to second order accuracy, even in the stiff regime. The gas velocity solution is in fact the only quantity entering Eqs. (19) and (20). We have actually tried to employ more sophisticated approaches than Eq. (18), which would also involve the dust fluid velocity, but despite the higher degree of complexity and computational cost, they did not improve on the algorithm accuracy.

3. Two-fluid semi-implicit predictor–corrector

3.1. Two-fluid description

In order to efficiently model the collective effect of the drag force exerted by the dust particles on the fluid we use a fluid like description of the dust component. Thus, using a particle–mesh method we define the dust density and velocity field on a Cartesian grid as

$$\rho_d(\mathbf{i}) = \frac{1}{\Delta x^3} \sum_p w[x_p - x(\mathbf{i})] m_p, \tag{21}$$

$$u_d(\mathbf{i}) = \sum_p w[x_p - x(\mathbf{i})]\, v_p, \tag{22}$$

where as in the previous section $w(s)$ is a weight function, $x(\mathbf{i})$, is the $\mathbf{i}$-th cell's center, but now the summation is carried out over all the dust particles. Note that the position and velocity of the dust particles are updated independently at each time-step using a particle method described in Section 2. The time evolution of ρ_d and $\rho_d u_d$ is then obtained from the zero-th and first velocity moments, respectively, of Boltzmann's equation for the dust distribution function, $g_d(x, v, t)$. Using the particle equation of motion (3) and (4), and the appropriate collision term we obtain

$$\frac{\partial \rho_d}{\partial t} + \frac{\partial}{\partial x}(\rho_d u_d) = 0, \tag{23}$$

$$\frac{\partial}{\partial t}(\rho_d u_d) + \frac{\partial}{\partial x}(\rho_d u_d u_d) = -\rho_d \kappa_d (u_d - u_g) - \rho_d \nabla\phi, \tag{24}$$

where closure is granted by neglecting higher order velocity terms as suggested by [13]. However, different closures can in principle be employed starting from the particle description as need be. Finally, by Newton's third Law, Eq. (24) indicates that the collective drag force exerted on the gas by the dust particles ought to be

$$f_d = -\kappa_g (u_g - u_d), \kappa_g = \kappa_d \frac{\rho_d}{\rho_g}, \tag{25}$$

ensuring momentum conservation.

We can now extend the set of conservative variables, U, to include the density and momentum of the dust component,

$$U = (\rho, \rho u_g, \rho E)^T \rightarrow (\rho_g, \rho_g u_g, \rho E, \rho_d, \rho_d u_d)^T. \tag{26}$$

The extended set of equations for U is obtained by combining (1), (2), (23) and (24). After rearranging the source terms, it reads

$$\frac{\partial U}{\partial t} + \frac{\partial F(U)}{\partial x} = K_U U + S(U), \tag{27}$$

where

$$F(U) = \begin{pmatrix} \rho u_g \\ \rho u_g^2 + P \\ u_g\,[\rho E + P] \\ \rho u_d \\ \rho u_d^2 \end{pmatrix}, \quad S(U) = \begin{pmatrix} 0 \\ \rho_g \nabla\phi \\ u_g \rho_g \nabla\phi \\ 0 \\ \rho_d \nabla\phi \end{pmatrix}, \quad K_U = \begin{pmatrix} 0 & 0 & 0 & 0 & 0 \\ 0 & -\kappa_g & 0 & 0 & \kappa_d \\ 0 & 0 & 0 & 0 & 0 \\ 0 & 0 & 0 & 0 & 0 \\ 0 & \kappa_g & 0 & 0 & -\kappa_d \end{pmatrix}. \tag{28}$$

3.2. Semi-implicit method

Given our extended system of Eq. (27) we aim for a scheme in which an explicit approach is retained for the non-stiff conservative hydrodynamic term, $\nabla \cdot F$, and a semi-implicit method is employed for the stiff part of the source terms.

As in Miniati and Colella [19], our time-discretization for the source terms is a single-step, second order accurate scheme. However, instead of a method based on the deferred correction approach [9], here we derive our predictor corrector using again the α-QSS [21]. The reason is that although stable and convergent, unlike the α-QSS method, the deferred correction method is not L-stable (although a combination of two such methods can lead to L-stability). This can lead to large errors, particularly with regard to momentum conservation, in a hybrid method in which fluid and particles are stiffly coupled.

Our semi-implicit method consists in solving the following collection of ODEs, one at each grid point,

$$\frac{dU}{dt} = K_U U + S(U) - (\nabla \cdot \vec{F})^{n+\frac{1}{2}}, \tag{29}$$

where we view the time-centered flux divergence as a constant source, whose computation using a modified Godunov method is described below. Our predictor–corrector step then reads:

$$\widetilde{U}(t_0 + \Delta t) = e^{K_0 \Delta t} U_0 + \mathcal{I}^0_{K_0}(\Delta t)\left[S(U_0) - (\nabla \cdot \vec{F})^{n+\frac{1}{2}}\right]\Delta t, \tag{30}$$

$$U(t_0 + \Delta t) = e^{\overline{K} \Delta t} U_0 + \mathcal{I}^0_{\overline{K}}(\Delta t)\left[S(U_0) - (\nabla \cdot \vec{F})^{n+\frac{1}{2}}\right]\Delta t + \mathcal{I}^1_{\overline{K}}(\Delta t)\frac{S(\widetilde{U}) - S(U_0)}{\Delta t}\frac{\Delta t^2}{2}, \tag{31}$$

where, $\overline{K} \equiv [K(U_0) + K(\widetilde{U})]/2$, is used in Eq. (31), and we have defined the set of operators

$$\mathcal{I}^n_Q(t) \equiv \frac{n!}{t^n}\int_0^t e^{(t-\tau)Q}\tau^n d\tau. \tag{32}$$

Note that gravity is actually unaffected by the operators $\mathcal{I}^n_Q(t)$; however the form of Eqs. (30) and (31) is suitable for a more general form of $S(U)$, which may even include stiff terms associated, for example, with an endothermic source.[1] Although the form of predictor corrector in the above equations appears different from the original system (11) and (12), their equivalence can be easily verified by replacing the operators K, Q with the coefficients p, q. It is also easy to see that in the non-stiff limit, the above scheme reduces to the usual second order accurate explicit formulation

$$U(t_0 + \Delta t) = (1 + \overline{K}\Delta t)U_0 - \Delta t\,(\nabla \cdot F)^{n+\frac{1}{2}} + \frac{\Delta t}{2}\left[S(\widetilde{U}) + S(U_0)\right]. \tag{35}$$

4. Two-fluid predictor step

In order to compute our predictor step, we cast the extended two-fluid gas–dust system in primitive form as follows:

$$\frac{\partial W}{\partial t} + A(W)\frac{\partial W}{\partial x} = K W + G, \tag{36}$$

[1] In this case, if Σ indicates the endothermic source, Eq. (29), as well as Eqs. (30) and (31), should be modified by replacing

$$S(U) \leftarrow S(U) + \Sigma(U_0), \tag{33}$$
$$K(U) \leftarrow K(U) + \nabla_U \Sigma(U). \tag{34}$$

where the primitive variables are

$$W = (\rho_g, u_g, P, \rho_d, u_d)^T, \tag{37}$$

and the quasi-linear operator, $A(W) \equiv \nabla_U W \cdot \nabla_U F \cdot \nabla_W U$, which includes an advection and a Lagrangian component, is

$$A(W) \equiv u_g \mathrm{I} + A_L, A_L = \begin{pmatrix} 0 & \rho_g & 0 & 0 & 0 \\ 0 & 0 & \rho_g^{-1} & 0 & 0 \\ 0 & \rho_g c^2 & 0 & 0 & 0 \\ 0 & 0 & 0 & (u_d - u_g) & \rho_d \\ 0 & 0 & 0 & 0 & (u_d - u_g) \end{pmatrix}. \tag{38}$$

Finally

$$K = \begin{pmatrix} 0 & 0 & 0 & 0 & 0 \\ 0 & -\kappa_g & 0 & 0 & \kappa_g \\ 0 & 0 & 0 & 0 & 0 \\ 0 & 0 & 0 & 0 & 0 \\ 0 & \kappa_d & 0 & 0 & -\kappa_d \end{pmatrix}, \quad G = \begin{pmatrix} 0 \\ -\nabla\phi \\ 0 \\ 0 \\ -\nabla\phi \end{pmatrix}, \tag{39}$$

represent the drag operator and the residual source term, including gravity, in primitive form. Following the method in Miniati and Colella [19] we can follow the dynamics of the system along Lagrangian trajectories

$$\frac{DW}{Dt} = -A_L(W)\frac{\partial W}{\partial x} + KW + G, \tag{40}$$

with solution given by Duhamel's formula:

$$W(t) = e^{Kt}W(0) - \int_0^t e^{K(t-\tau)}\left[A_L\frac{\partial W}{\partial x} - G\right]d\tau. \tag{41}$$

This allows us to define a modified dynamics reading

$$\frac{DW}{Dt} + \mathcal{I}_K(t)A_L\frac{\partial W}{\partial x} = \mathcal{I}_K(t)[KW(0) + G] + O(t). \tag{42}$$

4.1. Characteristic analysis

We use the quasi-linear system (42) with $t = \Delta t/2$ to compute the Godunov predictor step. Thus we analyze the modified hyperbolic structure of that system of equations.

With the choice of K in (39), from Eq. (32) we obtain

$$e^{K\Delta t/2} = \begin{pmatrix} 1 & 0 & 0 & 0 & 0 \\ 0 & \frac{\kappa_d + \kappa_g e^{-\kappa\Delta t/2}}{\kappa} & 0 & 0 & \frac{\kappa_g(1-e^{-\kappa\Delta t/2})}{\kappa} \\ 0 & 0 & 1 & 0 & 0 \\ 0 & 0 & 0 & 1 & 0 \\ 0 & \frac{\kappa_d(1-e^{-\kappa\Delta t/2})}{\kappa} & 0 & 0 & \frac{\kappa_g + \kappa_d e^{-\kappa\Delta t/2}}{\kappa} \end{pmatrix}, \tag{43}$$

where $\kappa = \kappa_g + \kappa_d$ is the total relaxation rate, and

$$\mathcal{I}_K(\Delta t/2) = \begin{pmatrix} 1 & 0 & 0 & 0 & 0 \\ 0 & \frac{\kappa_d + \beta\kappa_g}{\kappa} & 0 & 0 & \frac{\kappa_g(1-\beta)}{\kappa} \\ 0 & 0 & 1 & 0 & 0 \\ 0 & 0 & 0 & 1 & 0 \\ 0 & \frac{\kappa_d(1-\beta)}{\kappa} & 0 & 0 & \frac{\kappa_g + \beta\kappa_d}{\kappa} \end{pmatrix}, \tag{44}$$

where

$$\beta = \beta\left(\frac{\kappa\Delta t}{2}\right) = \frac{1 - e^{-\frac{1}{2}\kappa\Delta t}}{\frac{1}{2}\kappa\Delta t}, \quad 0 < \beta < 1. \tag{45}$$

We can then define the modified linear operator

$$\mathcal{I}_K(\Delta t/2)A_L = A_L^{\rm eff} = \begin{pmatrix} 0 & \rho_g & 0 & 0 & 0 \\ 0 & 0 & \frac{\kappa_d+\beta\kappa_g}{\kappa\rho_g} & 0 & \frac{\kappa_g(1-\beta)}{\kappa}(u_d-u_g) \\ 0 & \rho_g c^2 & 0 & 0 & 0 \\ 0 & 0 & 0 & (u_d-u_g) & \rho_d \\ 0 & 0 & \frac{\kappa_d(1-\beta)}{\kappa\rho_g} & 0 & \frac{\kappa_g+\beta\kappa_d}{\kappa}(u_d-u_g) \end{pmatrix}, \tag{46}$$

with associated characteristic equation

$$\lambda[\lambda-(u_d-u_g)]\left[\lambda^3-\lambda^2\frac{\kappa_g+\beta\kappa_d}{\kappa}(u_d-u_g)-\lambda\frac{\kappa_d+\beta\kappa_g}{\kappa}c^2+\beta c^2(u_d-u_g)\right]=0. \tag{47}$$

The system eigenvalues are given by the roots of the above equation. The first obvious solution, $\lambda^0=0$, correspond to an entropy wave for the gas component. Since an entropy wave does not involve velocity perturbations, we expect this type of wave to be unaffected by the presence of a drag term. The other obvious eigenvalue, $\lambda^d=(u_d-u_g)$, is the equivalent of an entropy wave, but for the dust component. Perturbations in ρ_d propagate only along the characteristic curve associated to this eigenvalue and, therefore, do not affect other primitive variables. For this reason, in the following we simplify the characteristic analysis by dropping out the ρ_d components and assume that: ρ_d is transported as a passive scalar with speed λ^d and its intermediate state Riemann solution is simply given by the average of left and right state values.

The remaining eigenvalues of the system are given by the roots of the cubic polynomial appearing in Eq. (47), which can be shown to be always distinct and real, with a few exceptions discussed below. The set of relevant eigenvalues is then

$$\lambda^0=0, \tag{48}$$

$$\lambda^+=\frac{1}{3}\hat{\delta u}+\frac{2}{\sqrt{3}}\left(\hat{c}^2+\frac{\hat{\delta u}^2}{3}\right)^{1/2}\cos\left(\frac{\varphi}{3}\right), \tag{49}$$

$$\lambda^-=\frac{1}{3}\hat{\delta u}+\frac{2}{\sqrt{3}}\left(\hat{c}^2+\frac{\hat{\delta u}^2}{3}\right)^{1/2}\cos\left(\frac{\varphi}{3}+\frac{2}{3}\pi\right), \tag{50}$$

$$\lambda^\times=\frac{1}{3}\hat{\delta u}+\frac{2}{\sqrt{3}}\left(\hat{c}^2+\frac{\hat{\delta u}^2}{3}\right)^{1/2}\cos\left(\frac{\varphi}{3}+\frac{4}{3}\pi\right), \tag{51}$$

where

$$\hat{c}=\sqrt{\frac{\kappa_d+\beta\kappa_g}{\kappa}}c,\quad \hat{\delta u}=\frac{\kappa_g+\beta\kappa_d}{\kappa}\delta u,\quad \delta u=u_d-u_g, \tag{52}$$

$$\varphi=\cos^{-1}\left[\hat{\delta u}\frac{2\hat{\delta u}^2+9\hat{c}^2\left(1-\frac{3\beta\kappa^2}{(\kappa_d+\beta\kappa_g)(\kappa_g+\beta\kappa_d)}\right)}{2(3\hat{c}^2+\hat{\delta u}^2)^{\frac{3}{2}}}\right], \tag{53}$$

and $\cos^{-1}$ conventionally indicates the principal value of the multivalued inverse cosine function. With this convention we always have $\lambda^+>(\lambda^\times,\lambda^0)>\lambda^-$, whereas all three cases $\lambda^0\gtrless\lambda^\times$ are admitted. An extra eigen-mode driven by the dust drift has appeared. Under stiff dust–gas coupling conditions ($\beta<1$), this mode mixes with the pressure driven modes thus acquiring an acoustic-like character. Likewise, the properties of the original sound waves are contaminated by the dust component. The degree of mutual contamination is regulated by the 'mixing angle' φ. In general sound speed is affected by both the additional inertia and by the motion of the dust particles.

To see this in more details in the following we explore the asymptotic behavior of the waves in a few cases of interest. The general results are summarized in Fig. 1. In the non-stiff limit, we have

$$\lim_{\beta\to1}\lambda^+=c,\quad \lim_{\beta\to1}\lambda^-=-c,\quad \lim_{\beta\to1}\lambda^\times=\delta u, \tag{54}$$

thus recovering the expected values. However, as the dust particle drift vanishes we have

$$\lim_{\delta u\to0}\lambda^+=\hat{c},\quad \lim_{\delta u\to0}\lambda^-=-\hat{c},\quad \lim_{\delta u\to0}\lambda^\times=\frac{\beta\kappa}{\kappa_d+\beta\kappa_g}\hat{\delta u}. \tag{55}$$

Here $\hat{c}$ is given in Eq. (52) and correspond to a sound speed in which the gas density is replaced by an effective average between the dust and the gas densities. So, in the stiff limit ($\beta\to0$), it is the total density that enters the definition of the sound speed (which can be dominated by the dust density). Similarly, in the limit of large values of $\hat{\delta u}$ we obtain (see dashed lines in Fig. 1)

$$\lim_{\hat{\delta u}\to\infty}\lambda^+=\hat{\delta u},\quad \lim_{\hat{\delta u}\to\infty}\lambda^-=-\check{c},\quad \lim_{\hat{\delta u}\to\infty}\lambda^\times=\check{c}, \tag{56}$$

$$\lim_{\hat{\delta u}\to-\infty}\lambda^+=\check{c},\quad \lim_{\hat{\delta u}\to-\infty}\lambda^-=\hat{\delta u},\quad \lim_{\hat{\delta u}\to-\infty}\lambda^\times=-\check{c}, \tag{57}$$

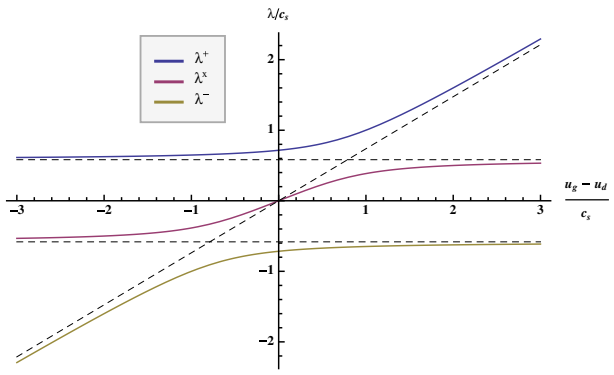

Fig. 1. Solid lines: eigenvalues versus $(u_g - u_d)$, in sound speed units, for $\beta = 0.25$ and $\kappa_g/\kappa = 0.65$. The dash lines indicate the various asymptotic branches corresponding to $\lambda = \check{c}$ (high, horizontal) $\lambda = -\check{c}$ (low horizontal) and $\lambda = \hat{\delta u}$ (diagonal).

where we have used

$$\check{c} = \sqrt{\frac{\beta\kappa}{\kappa_g + \beta\kappa_d}}c, \tag{58}$$

which represent an effective sound speed when the perturbation propagates opposite to the direction of the dust particles velocity. The said propagation speed vanishes in the stiff limit, but it always coincide with the sound speed (c) in the limit of negligible dust density (i.e. $\kappa_g \to 0, \kappa_d \to \kappa$).

To conclude the analysis we introduce the array of right eigenvectors (by column)

$$R \equiv \begin{pmatrix} 1 & 1 & 1 & 1 \\ \frac{\lambda^-}{\rho_g} & 0 & \frac{\lambda^\times}{\rho_g} & \frac{\lambda^+}{\rho_g} \\ c^2 & 0 & c^2 & c^2 \\ \frac{(\hat{c}-\lambda^-)(\hat{c}+\lambda^-)}{\mu\delta u(\beta-1)} & 0 & \frac{(\hat{c}-\lambda^\times)(\hat{c}+\lambda^\times)}{\mu\delta u(\beta-1)} & \frac{(\hat{c}-\lambda^+)(\hat{c}+\lambda^+)}{\mu\delta u(\beta-1)} \end{pmatrix}, \tag{59}$$

where, to simplify the notation, we have introduced the reduced density, $\mu \equiv \rho_g\rho_d/(\rho_g + \rho_d)$. Similarly, the array of left eigenvectors (by row) is

$$L \equiv \begin{pmatrix} 0 & -\frac{(\lambda^+ + \lambda^\times)\rho_g}{(\lambda^+ - \lambda^-)(\lambda^\times - \lambda^-)} & \frac{\hat{c}^2 + \lambda^+\lambda^\times}{c^2(\lambda^+ - \lambda^-)(\lambda^\times - \lambda^-)} & -\frac{\mu\delta u(\beta-1)}{(\lambda^+ - \lambda^-)(\lambda^\times - \lambda^-)} \\ 1 & 0 & -\frac{1}{c^2} & 0 \\ 0 & \frac{(\lambda^+ + \lambda^-)\rho_g}{(\lambda^+ - \lambda^\times)(\lambda^\times - \lambda^-)} & -\frac{\hat{c}^2 + \lambda^+\lambda^-}{c^2(\lambda^+ - \lambda^\times)(\lambda^\times - \lambda^-)} & \frac{\mu\delta u(\beta-1)}{(\lambda^+ - \lambda^\times)(\lambda^\times - \lambda^-)} \\ 0 & -\frac{(\lambda^\times + \lambda^-)\rho_g}{(\lambda^+ - \lambda^-)(\lambda^+ - \lambda^\times)} & \frac{\hat{c}^2 + \lambda^\times\lambda^-}{c^2(\lambda^+ - \lambda^-)(\lambda^+ - \lambda^\times)} & -\frac{\mu(u_d - u_g)(\beta-1)}{(\lambda^+ - \lambda^-)(\lambda^+ - \lambda^\times)} \end{pmatrix}. \tag{60}$$

Just like for the eigenvalues, it can be easily verified that the definitions (59) and (60) tend to the usual expression for the left and right eigenvectors in the non-stiff limit.

4.1.1. Loss of strict hyperbolicity

When either one of the following three cases occurs, $\beta \to 1, \delta u \to 0, \mu \to 0$, (implying either $\rho_g = 0$ or $\rho_d = 0$) the first, third and fourth right eigenvectors, appear to become singular. However, the asymptotic analysis shows that in these limits the expressions, $\lambda^\pm \mp \hat{c}$, approach zero quadratically in $(\beta - 1)$ and linearly in both ρ_d and δu, so that the first and fourth right eigenvectors are always well defined.

While the third right eigenvector still diverges, the corresponding left eigenvector tends to zero at the same rate (because $\lambda^+ + \lambda^-$ is quadratic in $(\beta - 1)$ and linear in both ρ_d and δu, whereas $\hat{c}^2 + \lambda^+\lambda^-$, is quadratic in both $(\beta - 1)$ and δu, and linear in ρ_d), so that the characteristic decomposition is non-singular in the above limits. Note that this "illness" of the third right eigenvector could be formally cured by renormalizing the third left and right eigenvectors by the factor f_3 and f_3^{-1}, respectively, where

$$f_3 = \frac{(\lambda^+ - \lambda^\times)(\lambda^\times - \lambda^-)}{\mu\delta u(\beta - 1)}. \tag{61}$$

The eigensystem can still become singular when two eigenvalues become identical, i.e. strict hyperbolicity is lost. Inspection of Eqs. (49)–(51) and (53) indicates that it is possible to have $\lambda^- = \lambda^\times$ or $\lambda^+ = \lambda^\times$ when $\phi = 0$ or $\phi = \pi$, respectively. These relations are satisfied when $\delta\hat{u} = \mp\hat{c}$, respectively, and simultaneously either $\beta = 1$, or $\mu = 0$ is verified. As it appears from

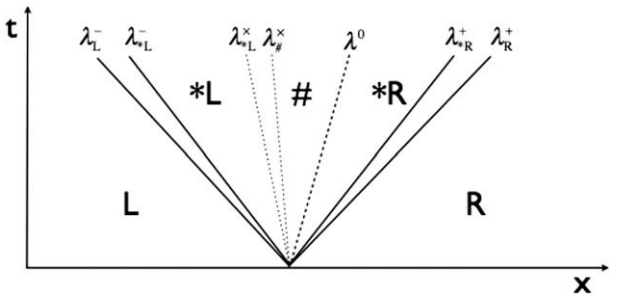

Fig. 2. Four-waves structure of the Riemann problem.

(59) and (60), in this case the third ($\times$) eigenvectors (left and right) become parallel to either the first ($-$) or fourth (+) eigenvectors, respectively.

When this is the case we modify our characteristic synthesis as suggested by Bell et al. [4]. For example, if $\alpha_k = \sum_k l_k \cdot \delta W$ are the coefficients of the characteristic decomposition of a perturbation δW with respect to the set of left eigenvalues l_k, when $\lambda^\times - \lambda^\pm \leqslant \epsilon$, with typically, $\epsilon \simeq 10^{-2}$, the above perturbation would be reconstructed as

$$\delta W = \sum_k \alpha_k r_k \to \alpha_\times r_\pm + \sum_{k\neq\times} \alpha_k r_k, \tag{62}$$

where r_k is the set of right eigenvectors.

4.1.2. Addition of endothermic processes

We can easily generalize the above results to include stiff endothermic processes. Suppose the rate of change of the gas internal energy, $e = P/\rho_g(\gamma-1)$, is

$$\frac{de}{dt} = \Lambda(e,\rho_g). \tag{63}$$

In this case the modified linear operator defined in Eq. (46) becomes

$$A_L^{\rm eff} = \begin{pmatrix} 0 & \rho_g & 0 & 0 & 0 \\ 0 & 0 & \frac{\kappa_d+\beta\kappa_g}{\kappa\rho_g} & 0 & \frac{\kappa_g(1-\beta)}{\kappa}(u_d-u_g) \\ 0 & \alpha\rho_g c^2 - \frac{(1-\alpha)\Lambda_\rho\rho_g}{\Lambda_e} & 0 & 0 & 0 \\ 0 & 0 & 0 & (u_d-u_g) & \rho_d \\ 0 & 0 & \frac{\kappa_d(1-\beta)}{\kappa\rho_g} & 0 & \frac{\kappa_g+\beta\kappa_d}{\kappa}(u_d-u_g) \end{pmatrix}, \tag{64}$$

where

$$\Lambda_e \equiv \frac{\partial\Lambda}{\partial e}, \quad \Lambda_\rho \equiv \frac{\partial\Lambda}{\partial\rho_g}, \quad \alpha(\Delta t) \equiv \frac{e^{\Lambda_e\Delta t}-1}{\Lambda_e\Delta t}, \quad 0<\alpha<1. \tag{65}$$

Then it can be shown that the above characteristic analysis remains valid provided the gas sound speed is replaced with the following *effective* value [19]:

$$c_{\rm eff} = \left\{\left[1+\alpha(\gamma-1)-(1-\alpha)\frac{\Lambda_\rho\rho_g}{\Lambda_e e}\right]\frac{P}{\rho_g}\right\}^{\frac{1}{2}}. \tag{66}$$

As discussed at length in [19] the above scheme is applicable as long as the fluid is thermally stable [10], namely:

$$\frac{\Lambda_e e}{\Lambda_\rho\rho_g} > \frac{1-\alpha}{\alpha(\gamma-1)+1}. \tag{67}$$

4.2. Linearized riemann solver

The characteristic analysis derived in Section 4.1 defines the structure of the solution to the Riemann problem for the gas–dust system. Unlike ordinary hydrodynamics, this is now characterized by three acoustic wave families and one entropy wave propagating at the fluid velocity.[2] The corresponding four characteristic curves determine in general five distinct

[2] For the sake of clarity, in the following we continue to ignore the contact discontinuity in the dust component, which travels at speed λ^d without interacting with the rest of the primitive variables.

regions, corresponding to the initial left (L) and right (R) states and three intermediate states of the gas. Fig. 2 illustrates this, for the case in which $\lambda^\times < \lambda^0$. In the $x-t$ plane, the solution cone is separated by the unperturbed R and L-states by the fastest and slowest eigenvalues, respectively. The R-state is connected to a *R-state by a rarefaction fan or a shock depending on whether λ_R^+ is faster or slower than λ_{*R}^+. The same applies to the connection between the L-state and *L-state. Then if $\lambda^\times < \lambda^0$ as assumed in Fig. 2, the *R-state is connected to a #-state by an ordinary contact discontinuity, where the density jumps but pressure and velocity remain constant. Finally, another acoustic wave separates the #-state and *L-state, which again either takes the form of a shock or a rarefaction wave depending on whether the characteristics with speed $\lambda_{*L}^\times$ and $\lambda_\#^\times$ converge or diverge.

In order to calculate the intermediate states described above, we use a linearized Riemann solver [27], which is discussed in detail below. Then, in general, given the input left and right states W_L, W_R, we can use the left and right eigenvectors, $\{l_k, r_k\}_{k=1,\dots,n}$ and the corresponding eigenvalues λ^k, computed at some intermediate state, to decompose the perturbation along the characteristics as follows:

$$\alpha^k = l^k \cdot (W_R - W_L),$$
$$W_R^k = W_L + \sum_{k'=1}^{k} \alpha_{k'} r_{k'}, W_L^k = W_R^k - \alpha_k r_k, \lambda_{L,R}^k = \lambda^k\left(W_{L,R}^k\right).$$

Then the solution to the Riemann problem along the ray $x/t = 0, W_{RP}$, is given by

$$W_{RP} = W_L + \sum_{\max\left(\lambda_L^k, \lambda_R^k\right)<0} \alpha_k r_k + \sum_{\lambda_L^k>0>\lambda_R^k, \lambda_L^k+\lambda_R^k<0} \alpha_k r_k + \sum_{\lambda_L^k<0<\lambda_R^k} \frac{\lambda_L^k}{\lambda_L^k - \lambda_R^k} \alpha_k r_k.$$

The first sum is the correction to the state for the waves that are unambiguously have a negative speed; the second is a correction to the state for transonic shocks; and the third a correction for transonic rarefactions, that prevents the formation of entropy-violating shocks. In the following we use a slight variation of this approach that is better able to preserve reflection symmetries.

Recall that we have three acoustic-like wave families $k = +, -, \times$ with speeds λ^k given in (49)–(51) and the remaining wave propagates at the fluid speed, λ^0. Assume for the moment that we can compute the eigenvalues λ^k at the intermediate states, *L,#, *R, following a procedure described in detail below. Then the approximate Riemann solver is given as follows.

If $\lambda^0 > 0$, then
if $\min\left(\lambda_{*L}^\times, \lambda_\#^\times\right) > 0$ or $\lambda_{*L}^\times > 0 > \lambda_\#^\times$ and $\lambda_{*L}^\times + \lambda_\#^\times > 0$ then

$$W_{RP} = \begin{cases} W_{*L} \text{ if } \max\left(\lambda_L^-, \lambda_{*L}^-\right) < 0 \text{ or } \lambda_L^- > 0 > \lambda_{*L}^-, \lambda_L^- + \lambda_{*L}^- < 0 \\ W_L + \frac{\lambda_L^-}{\lambda_L^- - \lambda_{*L}^-}(W_{*L} - W_L) \text{ if } \lambda_L^- < 0 < \lambda_{*L}^- \\ W_L \text{ otherwise} \end{cases}$$

else if $\lambda_{*L}^\times < 0 < \lambda_\#^\times$ then
$W_{RP} = W_{*L} + \frac{\lambda_{*L}^\times}{\lambda_{*L}^\times - \lambda_\#^\times}(W_\# - W_{*L})$
else
$W_{RP} = W_\#$
endif
else if $\lambda^0 < 0$, then
if $\max\left(\lambda_\#^\times, \lambda_{*R}^\times\right) < 0$ or $\lambda_\#^\times > 0 > \lambda_{*R}^\times$ and $\lambda_\#^\times + \lambda_{*R}^\times < 0$ then

$$W_{RP} = \begin{cases} W_{*R} \text{ if } \max(\lambda_{*R}^+, \lambda_R^+) > 0 \text{ or } \lambda_R^+ > 0 > \lambda_R^+, \lambda_{*R}^+ + \lambda_R^+ > 0 \\ W_R + \frac{\lambda_R^+}{\lambda_R^+ - \lambda_{*R}^+}(W_{*R} - W_R) \text{ if } \lambda_{*R}^+ < 0 < \lambda_R^+ \\ W_R \text{ otherwise} \end{cases}$$

else if $\lambda_\#^\times < 0 < \lambda_{*R}^\times$ then
$W_{RP} = W_{*R} + \frac{\lambda_{*R}^\times}{\lambda_{*R}^\times - \lambda_\#^\times}(W_\# - W_{*R})$
else
$W_{RP} = W_\#$
endif
endif

In order to complete our description of the approximate Riemann solver, we now outline the method for computing the intermediate states. Basically we integrate the characteristic equations along the characteristic directions to relate the jumps experienced by the primitive variables across adjacent states [12]. The characteristic directions are assumed to be constant and are computed at the foot of the characteristics. The characteristic equations are obtained by setting $l^k \cdot dW = 0$ for each eigenstate and they read

$$dp - \chi_g^-(\lambda^\times,\lambda^+)du_g - \chi_d^-(\lambda^\times,\lambda^+)du_d = 0, \tag{68}$$

$$dp - c^2 d\rho_g = 0, \tag{69}$$

$$dp - \chi_g^\times(\lambda^-,\lambda^+)du_g - \chi_d^\times(\lambda^-,\lambda^+)du_d = 0, \tag{70}$$

$$dp - \chi_g^+(\lambda^\times,\lambda^-)du_g - \chi_d^+(\lambda^\times,\lambda^-)du_d = 0, \tag{71}$$

where the characteristic slopes in phase–space are given by

$$\chi_g^+(\lambda^\times,\lambda^-) = \frac{\lambda^- + \lambda^\times}{\hat{c}^2 + \lambda^-\lambda^\times}\rho_g c^2, \tag{72}$$

$$\chi_d^+(\lambda^\times,\lambda^-) = \frac{\mu\delta u(-1+\beta)}{\hat{c}^2 + \lambda^-\lambda^\times}c^2, \tag{73}$$

and the analogous expressions for $\chi_{g,d}^-, \chi_{g,d}^\times$ are obtained by permutation of the symbols $+, -, \times$ in the above equations.

The above procedure of integrating the characteristic equations yields 12 equations in 12 variables. However, neither the gas or dust fluid velocities nor the gas pressure change across the contact discontinuity, reducing the system to 9 equations in the following 9 variables: $\rho_{g,*L}, u_{g,*L}, P_{g,*L}, u_{d,*L}, \rho_{g,*R}, u_{g,*R}, P_{g,*R}, u_{d,*R}, \rho_{g,\#}$, with $u_{g,\#}, P_{g,\#}, u_{d,\#}$ coinciding with the corresponding variable of either the *L or *R-state. In order to keep the system linear we make two further approximations when computing the characteristic directions (72) and (73) in the intermediate states: (1) we assume that the gas–dust velocity difference, $u_g - u_d$, in the intermediate *L, *R-states, can be approximated with the values corresponding to the L,R-states, respectively. And (2), that, when connecting the #-state with the *L-state (*R-state) via the -(+) characteristic, i.e. when $\lambda^\times < \lambda^0$ ($\lambda^\times > \lambda^0$), we can use the density of the *L-state (*R-state) instead of the value corresponding to the #-state. With this latter approximation the relations between velocity jumps across the characteristic line $\times$, remain unchanged whether $\lambda^\times < \lambda^0$ or $\lambda^\times > \lambda^0$. The solution then reads

$$u_{g,*R} = u_{g,R} + \frac{(P_L - P_R)\left(1 - \frac{\eta_L}{\eta_*}\right) + (u_{g,L} - u_{g,R})\left(\theta_L + \frac{\theta_*}{\eta_*}\eta_L\right) + (u_{d,L} - u_{d,R})\frac{\theta_* + \theta_L}{\eta_*}}{(\theta_L - \theta_R) - \eta_R\frac{\theta_L + \theta_*}{\eta_*} + \eta_L\frac{\theta_R + \theta_*}{\eta_*}}, \tag{74}$$

$$P_{*R} = P_R + \theta_R(u_{g,R} - u_{g,*R}), \tag{75}$$

$$u_{d,*R} = u_{d,R} + \eta_R(u_{g,R} - u_{g,*R}), \tag{76}$$

$$\rho_{g,*R} = \rho_{g,R} + \frac{P_{*R} - P_R}{c_R^2}, \tag{77}$$

$$u_{g,*L} = u_{g,L} + \frac{(P_L - P_R)\left(1 - \frac{\eta_R}{\eta_*}\right) + (u_{g,L} - u_{g,R})\left(\theta_R + \frac{\theta_*}{\eta_*}\eta_R\right) + (u_{d,L} - u_{d,R})\frac{\theta_* + \theta_R}{\eta_*}}{(\theta_L - \theta_R) - \eta_R\frac{\theta_L + \theta_*}{\eta_*} + \eta_L\frac{\theta_R + \theta_*}{\eta_*}} \tag{78}$$

$$P_{*L} = P_L + \theta_L(u_{g,L} - u_{g,*L}), \tag{79}$$

$$u_{g,*L} = u_{g,L} + \eta_L(u_{g,L} - u_{g,*L}), \tag{80}$$

$$\rho_{g,*L} = \rho_{g,L} + \frac{P_{*L} - P_L}{c_L^2}, \tag{81}$$

$$\rho_{g,\#} = \begin{cases} \rho_{g,*R} + \frac{P_{*L} - P_{*R}}{c_{*R}^2} & \text{if } \lambda_{*L}^\times > \lambda^0, \\ \rho_{g,*L} + \frac{P_{*R} - P_{*L}}{c_{*L}^2} & \text{if } \lambda_{*R}^\times < \lambda^0, \end{cases} \tag{82}$$

$$\rho_{d,*L} = \rho_{d,*R} = \rho_{d,\#} = \frac{\rho_{d,L} + \rho_{d,R}}{2}, \tag{83}$$

where we have defined the following coefficients,

$$\theta_R = \frac{\chi_{g,R}^-\chi_{d,R}^\times - \chi_{g,R}^\times\chi_{d,R}^-}{\chi_{d,R}^- - \chi_{d,R}^\times} = -\left(\frac{\rho_g c^2}{\lambda^+}\right)_R, \quad \theta_L = \frac{\chi_{g,L}^+\chi_{d,L}^\times - \chi_{g,L}^\times\chi_{d,L}^+}{\chi_{d,L}^+ - \chi_{d,L}^\times} = -\left(\frac{\rho_g c^2}{\lambda^-}\right)_L, \tag{84}$$

$$\eta_R = \frac{\chi_{g,R}^- - \chi_{g,R}^\times}{\chi_{d,R}^- - \chi_{d,R}^\times} = \left[\frac{\rho_g}{\lambda^+}\frac{(\lambda^+)^2 - \hat{c}^2}{\mu\delta u(\beta - 1)}\right]_R, \quad \eta_L = \frac{\chi_{g,L}^+ - \chi_{g,L}^\times}{\chi_{d,L}^+ - \chi_{d,L}^\times} = \left[\frac{\rho_g}{\lambda^-}\frac{(\lambda^-)^2 - \hat{c}^2}{\mu\delta u(\beta - 1)}\right]_L, \tag{85}$$

$$\theta_* = \frac{\chi_{g,*R}^-\chi_{d,*L}^+ - \chi_{g,*L}^+\chi_{d,*R}^-}{\chi_{d,*L}^+ - \chi_{d,*R}^-}, \quad \eta_* = \frac{\chi_{g,*L}^+ - \chi_{g,*R}^-}{\chi_{d,*L}^+ - \chi_{d,*R}^-}. \tag{86}$$

The extra symbols L, *L, *R, R in the subscript of the χ functions defined in (72) and (73) indicate the state at which the characteristic directions is defined. Note that while the definition of the coefficients $\theta_L, \theta_R, \eta_L, \eta_R$ is based on the known L, R-states, computing θ_* and η_* involves knowledge of the intermediate states, *L or *R. It was in order to avoid the non-linearities arising from such dependencies that we have introduced the above approximations (1) and (2).

As a sanity check we may note that the non-stiff limit for the characteristic slopes in phase–space read

$$\lim_{\beta\to 1}\chi_g^{\pm}=\mp\rho c,\quad \lim_{\beta\to 1}\chi_d^{\pm},\chi_g^{\times}=0,\quad \lim_{\beta\to 1}\chi_d^{\times}=\infty, \tag{87}$$

so that the coefficients in (84) and (86) tend to

$$\lim_{\beta\to 1}\theta_L=\rho_L c_L,\quad \lim_{\beta\to 1}\theta_R=-\rho_R c_R,\quad \lim_{\beta\to 1}\theta_*=\text{const.},\quad \lim_{\beta\to 1}\eta_{L,R}=0,\quad \lim_{\beta\to 1}\eta_*=\infty, \tag{88}$$

and the Riemann solver solutions (74) and (83) reduce to the usual expressions [12].

4.3. Godunov predictor in one dimension

With the operator A^{eff} and the sets of left and right eigenvectors that we have worked out in Section 4.1, the Godunov predictor step is carried out as usual as follows. First the local slopes are defined. In particular at each point left and right one-sided slopes as well as cell centered slopes are evaluated and then a final choice on the local slope ΔW_i is defined by using van Leer limiter. The upwind, time-averaged left $(-)$ and right $(+)$ states at cell interfaces due to fluxes in the normal direction, q, are then reconstructed as:

$$W_{i,\pm,q}=W_i^n+\frac{1}{2}\left(I-\frac{\Delta t}{\Delta x}A_i^{\text{eff}}\right)P_{\pm}(\Delta W_i), \tag{89}$$

where

$$P_{\pm}(W)=\sum_{\pm\lambda_k>0}(l_k\cdot W)\cdot r_k. \tag{90}$$

The source term component is likewise accounted for as

$$W_{i,\pm,q}=W_{i,\pm,q}+\frac{\Delta t}{2}\mathcal{I}_K^0(\Delta t/2)S. \tag{91}$$

The fluxes at the cell faces $F_{i+\frac{1}{2}}$ are computed by solving the Riemann problem with left and right states given by $(W_{i,+},W_{i+1,-})$ to obtain $W_{i+\frac{1}{2}}^{n+\frac{1}{2}}$ and computing $F_{i+\frac{1}{2}}=F\left(W_{i+\frac{1}{2}}^{n+\frac{1}{2}}\right)$.

To modify this procedure to account for the effective dynamics, we use the characteristic analysis of the effective dynamics to perform each of the three steps. The projection operator and any limiting in characteristic variables is done using the eigenvectors and eigenvalues for the effective dynamics derived in Section 4.1. Finally, the approximate Riemann solvers we use was defined in Section 4.2.

4.4. Extension to more than one dimension

For directionally unsplit schemes in D dimensions an additional step is required in order to correct the time-averaged left/right states at cell interfaces, $W_{i,\pm,d}$ in Eq. (91), for the effects of $D-1$ fluxes perpendicular to the cell interface normal direction. Based on Eq. (42) the effect of the stiff source term would be accounted for by carrying out for each additional direction, q, a transformation

$$A_q\to\mathcal{I}_K^0(\Delta t/2)A_{L,q}+u_q\mathrm{I}\equiv A_q^{\text{eff}}, \tag{92}$$

analogous to that described in Eq. (46). In the method proposed by [7,25] the corrections due to transverse fluxes are computed according to a conservative scheme. For example in two dimensions,[3] with $q=x$

$$W_{i,j,\pm,x}=W_{i,j,\pm,x}-\frac{\Delta t}{2\Delta y}\nabla_U W\left(F^y_{i,j+\frac{1}{2}}-F^y_{i,j-\frac{1}{2}}\right), \tag{93}$$

where the input $W_{i,j,\pm,x}$ is computed using a one-dimensional Godunov calculation as in the previous section, as are the fluxes $F^y_{i,j+\frac{1}{2}}$. The above transformations imply the following transverse flux corrections for the gas and dust velocity, $\delta u_g,\delta u_v$, respectively:

$$\delta u_{g,x}\to\delta u_{g,x}+\frac{\Delta t}{2\Delta y}\frac{\kappa_g}{\kappa}(1-\beta)\left[\frac{p_{i,j+\frac{1}{2}}-p_{i,j-\frac{1}{2}}}{\rho_g}-(u_d-u_g)\left(u_{y,i,j+\frac{1}{2}}-u_{y,i,j-\frac{1}{2}}\right)\right], \tag{94}$$

$$\delta u_{d,x}\to\delta u_{d,x}-\frac{\Delta t}{2\Delta y}\frac{\kappa_d}{\kappa}(1-\beta)\left[\frac{p_{i,j+\frac{1}{2}}-p_{i,j-\frac{1}{2}}}{\rho_g}-(u_d-u_g)\left(u_{y,i,j+\frac{1}{2}}-u_{y,i,j-\frac{1}{2}}\right)\right], \tag{95}$$

where, unless explicitly indicated, all quantities are evaluated at cell center, i,j.

[3] Notation in Eq. (93) indicates that primitive variables are converted into conservative variables which are then updated through conservative fluxes and then converted back into primitive form.

5. Stability considerations

The stability properties of the above modified Godunov's method are analogous to those discussed in [19] when considering endothermic source terms. In particular we note that the inspection of the characteristic analysis shows that the *sub-characteristic condition* for the characteristic speeds at equilibrium is always satisfied. This condition, while being necessary for the stability of our linearized system [27], also guarantees that the numerical solution tends to the solution of the equilibrium equation as the relaxation time tends to zero [6].

In addition, since the structure of the equations and the numerical framework, including the Riemann solver, remain fundamentally unaltered with respect to classic Godunov's schemes, we expect the usual stability conditions to apply, namely the familiar CFL condition on the time-step

$$\max(|\lambda_*|)\frac{\Delta t}{\Delta x} \leqslant 1, * = -, 0, \times, d, +. \tag{96}$$

As for the predictor corrector method described in Section 3.2, A-stability properties the α-QSS method have been discussed in detail by Mott et al. [21]. Although not specifically mentioned by the authors, the same stability analysis they present shows immediately that the α-QSS method is also L-stable.

6. Tests

6.1. Particle scheme

Before testing the convergence of the gas–dust scheme, we investigate the performance of the particle scheme presented in Section 2. For the purpose we consider an individual particle propagating through a medium with specified density, velocity and pressure distributions. As expected [21], our scheme reproduces the *exact* solution when the particle moves through a uniform medium, and when either the coupling constant or the background fluid has linear time dependence. Thus in the following for our testing purposes we use a non-linear time dependent density, velocity and pressure field corresponding to a one-dimensional, right propagating sound wave solution. Note that, although not presented here, we obtain equivalent convergence rates as shown below when an external force acting on the particle is included. The wave quantities denoted with a 'w' subscript are given by Landau and Lifshitz [17]

$$u_w(x,t) = u_{w,0} + B\sin\left\{x - u_{w,0}t - \left[c_0 + \frac{\gamma+1}{2}(u_w - u_{w,0})\right]t\right\}, \tag{97}$$

$$\rho_w(x,t) = \rho_{w,0}\left[1 + \frac{\gamma-1}{2}\frac{u_w}{c_0}\right]^{\frac{2}{\gamma-1}}, \quad P_w(x,t) = P_{w,0}\left[1 + \frac{\gamma-1}{2}\frac{u_w}{c_0}\right]^{\frac{2\gamma}{\gamma-1}}, \tag{98}$$

where, $c_0 = \sqrt{\frac{\gamma P_{w,0}}{\rho_{w,0}}}$, and we use

$$B = 10^{-2}, \quad u_{w,0} = 2, \quad \rho_{w,0} = 1, \quad P_{w,0} = 1, \quad \gamma = \frac{5}{3}. \tag{99}$$

Using the scheme described in Section 2 we advance the particle position and velocity to a solution time t_{end} using a progressively larger number of steps, N_{steps}, and a correspondingly smaller time-step, $\Delta t_N = t_{end}/N_{steps}$. We then estimate the error by comparing solutions with resolution different by a factor 2 and use Richardson extrapolation to measure the convergence rates. So, if $s(m)$ is the solution obtained using m time-steps, the convergence rate is given by

$$R(m) = \frac{\ln\left|\frac{s(m)-s(2m)}{s(2m)-s(4m)}\right|}{\ln(2)}. \tag{100}$$

In Table 1 we report results for a choice of the coupling constant κ_0 such that the propagation regime goes from mildly stiff to non-stiff. From left to right the table columns report the number of steps, the error and convergence rate of the particle position and velocity and, in the last column, the stiffness parameter, $\kappa_0\Delta t$. The scheme is clearly second order accurate over the stiffness range reported in the Table, even though the convergence rate of the velocity appears to be slower for small N_{steps}. However, this is not due to a decrease in convergence rate in the stiff regime. As illustrated in Table 2, the particle scheme is still second order accurate even for much larger values of the stiffness parameter.

6.2. Convergence rates in smooth flows

In this section we test the convergence of the method presented in this paper, by studying the propagation of small perturbations in a gas–dust system with a long and short drag relaxation timescale. We consider both a two-fluid method in which the dust is modeled as a fluid (and dust particles are not used), as well as the full fluid + particle method. In our test, the fluid component is initialized with uniform density, pressure and velocity values, except for a sinusoidal perturbation with small amplitude superposed to the x-velocity component. In formulae

Table 1
Particle scheme convergence rates.

N_{steps}	E_x	R_x	E_v	R_v	$\kappa_0\Delta t$
2	4.6E−3	1.4	8.1E−4	0.1	5.0E1
4	1.7E−3	2.2	7.8E−4	0.3	2.5E1
8	3.8E−4	2.2	6.5E−4	2.7	1.2E1
16	8.4E−5	2.0	1.0E−4	2.0	6.2E0
32	2.1E−5	2.0	2.5E−5	0.9	3.1E0
64	5.2E−6	2.0	1.4E−5	1.8	1.6E0
128	1.3E−6	2.0	4.0E−6	1.9	7.8E−1
256	3.2E−7	2.0	1.0E−6	2.0	3.9E−1
512	8.1E−8	2.0	2.6E−7	2.0	2.0E−1
1024	2.0E−8	2.0	6.6E−8	2.0	9.8E−2
2048	5.0E−9	2.0	1.7E−8	2.0	4.9E−2

Table 2
Particle scheme convergence rates.

N_{steps}	E_x	R_x	E_v	R_v	$\kappa_0\Delta t$
2	4.4E−3	1.3	9.4E−4	1.7	5.0E5
4	1.7E−3	2.2	2.9E−4	3.2	2.5E5
8	3.8E−4	2.2	3.1E−5	0.5	1.2E5
16	8.2E−5	2.0	2.2E−5	2.0	6.2E4
32	2.0E−5	2.0	5.5E−6	2.1	3.1E4
64	5.1E−6	2.0	1.2E−6	2.1	1.6E4
128	1.3E−6	2.0	2.8E−7	2.1	7.8E3
256	3.2E−7	2.0	6.6E−8	2.1	3.9E3
512	8.0E−8	2.0	1.6E−8	2.1	2.0E3
1024	2.0E−8	2.0	3.6E−9	2.3	9.8E2
2048	5.0E−9	2.0	7.4E−10	2.7	4.9E2

$$u_{g,x} = u_0\,[1 + A\cos(2\pi\mathbf{k}\cdot\mathbf{r} + \pi)], \tag{101}$$

$$\rho = \rho_0 = \gamma = 1.4, \quad p = p_0 = 0.5, \quad u_y = u_{y0} = 0.7, \quad u_0 = 0.5, \tag{102}$$

where $\mathbf{r}$ is the position vector. Similarly the dust particles are uniformly distributed on the grid in order to produce a uniform density, and their velocity is initialized as

$$u_{d,x} = u_0\,[1 + A\cos(2\pi\mathbf{k}\cdot\mathbf{r})], \tag{103}$$

that is half a period out of phase with respect to $u_{g,x}$. When testing the hybrid method in two dimensions we use 4 particles per cell and a we interpolate the particle quantities to the grid using a triangular-shape-cloud interpolation scheme [18].

The above initial conditions produce a sinusoidal wave with amplitude A propagating in the domain along the direction defined by the vector $\mathbf{k}$. While we have experimented with various values for the parameters $A, \mathbf{k}$ and κ_0, below we present results for a few cases only, summarized in Table 3. In particular we consider a perturbation amplitude $A = 1.4 \times 10^{-2}$ and adopt coupling coefficients $\kappa_0 = 1, 10^2, 10^6$ to explore the non-stiff and stiff regimes respectively and, for simplicity, we report only results from one-dimensional tests for the two-fluid model and from two-dimensional tests for the hybrid model.

In order to measure the rate at which the numerical solution converges, for each problem we carry out a set of 5 simulation runs employing $N_{cell} = 16, 32, 64, 128, 256$ for a total range of 32. Note that the stiffness conditions do not change significantly as the grid is refined within the range of resolutions considered here. The convergence rate is measured using Richardson extrapolation. Given the numerical solution q_r at a given resolution r we first estimate the error at a given point (i,j), as

$$\varepsilon_{r;i,j} = q_r(i,j) - \bar{q}_{r+1}(i,j), \tag{104}$$

where $\bar{q}_{r+1}$ is the solution at the next finer resolution, properly spatially averaged onto the coarser grid. We then take the n-norm of the error

$$L_n = \|\varepsilon_r\|_n = \left(\sum |\varepsilon_{r;i,j}|^n v_{i,j}\right)^{1/n}, \tag{105}$$

where, $v_{i,j} = \Delta x^2$ is the cell volume, and estimate the convergence rate as

$$R_n = \frac{\ln[L_n(\varepsilon_r)/L_n(\varepsilon_s)]}{\ln(\Delta x_r/\Delta x_s)}. \tag{106}$$

For each studied case listed in Table 3, we produce a corresponding Tables 4–7 reporting the L_1, L_2 and L_∞ norms of the error and the corresponding convergence rates, R_1, R_2 and R_∞, as defined above. Note that the convergence rate of the dust

Table 3
Run set.

Run	D	A	$\mathbf{k}$	κ_0	ρ_d/ρ_g	Note[a]
A	1	1.4×10^{-2}	(1,0)	1	1	two-fluid
B	1	1.4×10^{-2}	(1,0)	10^6	1	two-fluid
C	1	1.4×10^{-2}	(1,0)	10^6	10^{-3}	two-fluid
D	1	1.4×10^{-2}	(1,0)	10^6	10^3	two-fluid
E	1	1.4×10^{-2}	(1,0)	2×10^2	1	two-fluid
F	2	1.4×10^{-2}	$(2/\sqrt{5},1/\sqrt{5})$	1	1	hybrid
G	2	1.4×10^{-2}	$(2/\sqrt{5},1/\sqrt{5})$	10^6	1	hybrid
H	2	1.4×10^{-2}	$(2/\sqrt{5},1/\sqrt{5})$	10^6	10^{-3}	hybrid
I	2	1.4×10^{-2}	$(2/\sqrt{5},1/\sqrt{5})$	10^6	10^3	hybrid
L	2	1.4×10^{-2}	$(2/\sqrt{5},1/\sqrt{5})$	10^2	1	hybrid

[a] *Hybrid* = hydro + dust particles.

Table 4
Convergence rates: case: $A=1.4\times10^{-2}, \mathbf{k}=(1,0), \rho_d/\rho_g=1$.

N_{cells}	L_1	R_1	L_2	R_2	L_∞	R_∞	L_1	R_1	L_2	R_2	L_∞	R_∞
	density-gas						*x-vel-gas*					
16	6.4E−07	–	1.4E−06	–	4.1E−06	–	3.2E−06	–	7.1E−06	–	2.0E−05	–
32	1.6E−07	2.0	3.6E−07	2.0	1.0E−06	2.0	8.1E−07	2.0	1.8E−06	2.0	5.1E−06	2.0
64	4.0E−08	2.0	8.8E−08	2.0	2.5E−07	2.0	2.0E−07	2.0	4.5E−07	2.0	1.3E−06	2.0
128	9.9E−09	2.0	2.2E−08	2.0	6.3E−08	2.0	5.1E−08	2.0	1.1E−07	2.0	3.2E−07	2.0
	density-dust						*x-vel-dust*					
16	1.3E−05	–	2.9E−05	–	8.2E−05	–	4.6E−06	–	1.0E−05	–	2.9E−05	–
32	6.1E−06	1.1	1.4E−05	1.1	3.8E−05	1.1	1.2E−06	2.0	2.6E−06	2.0	7.2E−06	2.0
64	2.9E−06	1.0	6.5E−06	1.0	1.9E−05	1.0	2.9E−07	2.0	6.4E−07	2.0	1.8E−06	2.0
128	1.5E−06	1.0	3.2E−06	1.0	9.2E−06	1.0	7.2E−08	2.0	1.6E−07	2.0	4.5E−07	2.0

component is evaluated in a way analogous to the fluid components, i.e. by considering the convergence of the error of the fluid representation of the particles.

6.2.1. Two-fluid

Cases A–E test the performance of the two-fluid scheme in which the dust is fully treated as a fluid using the scheme described in Sections 3 and 4 and the particle scheme is not used. The five tests correspond to the following cases: (A) non-stiff, (B–D) stiff but with a range of dust-to-gas ratios and (E) mildly stiff case. In all tests the perturbation is along the x-axis, $\mathbf{k}=(1,0)$, although we have tested that the performance is the same in more than one dimension. The convergence rates for each case are reported in Tables 4 and 8, respectively, for the density and velocity of the gas and dust. Errors in the gas pressure are not reported but exhibit the same behavior. In the non-stiff case (A) all quantities converge with second order accuracy, except the dust density, which is somewhat expected since in the absence of drag a pressure-less fluid becomes singular. In the stiff cases (B–D), the scheme produces second order accurate results independent of the dust-to-gas ratio. In the intermediate regime, $\kappa_0\Delta t\sim 1$, the convergence rate is between first and second order accurate as expected theoretically [19]. Thus, the two-fluid algorithm for the dust–fluid system is second order accurate in both the stiff and non-stiff regimes, and somewhat less accurate in between.

6.2.2. Full scheme

Cases F–L test the performance of the full fluid + particle in which the dust is represented by a set of particles whose velocity and position are updated with the scheme described in Section 2. As in the previous section, the five tests correspond to the following cases: (F) non-stiff, (G–I) stiff but with a range of dust-to-gas ratios and (L) mildly stiff case. In all tests the perturbation is skewed with respect to the x-axis, $\mathbf{k}=(2,1)/\sqrt{5}$. The convergence rates for each case are reported in Tables 9–13, respectively, for all of the gas and dust variables.

Inspection of the reported tables shows that, as expected, in the non-stiff regime (Table 9) the error drops with second order accuracy, this time even for the dust density. In the stiff regime and, unless the fluid mass dominates over the dust mass, the error on the fluid quantities drops approximately with first order accuracy, see Table 10–12. Since, as illustrated in the Sections 6.1 and 6.2.1, both the particle scheme and the two-fluid scheme retain their second order accuracy irrespective of the stiffness conditions, the worsening in accuracy is most likely due to the difficulty of coupling the gas and the dust fully self-consistently in the stiff regimes. However, the scheme is stable and convergent, though only first order, which

Table 5
Convergence rates: case: $B = 1.4 \times 10^{-2}, \mathbf{k} = (1,0), \rho_d/\rho_g = 1$.

N_{cells}	L_1	R_1	L_2	R_2	L_∞	R_∞	L_1	R_1	L_2	R_2	L_∞	R_∞
	density-gas						*x-vel-gas*					
16	3.2E−06	–	7.1E−06	–	2.1E−05	–	9.3E−07	–	2.3E−06	–	9.6E−06	–
32	8.0E−07	2.0	1.8E−06	2.0	5.2E−06	2.0	2.1E−07	2.1	4.9E−07	2.2	2.3E−06	2.1
64	2.0E−07	2.0	4.4E−07	2.0	1.3E−06	2.1	5.7E−08	1.9	1.3E−07	1.9	4.5E−07	2.3
128	4.9E−08	2.0	1.1E−07	2.0	3.1E−07	2.0	1.6E−08	1.8	3.6E−08	1.8	1.2E−07	1.9
	density-dust						*x-vel-dust*					
16	3.7E−05	–	8.9E−05	–	4.0E−04	–	1.3E−06	–	2.9E−06	–	9.1E−06	–
32	1.0E−05	1.9	2.5E−05	1.8	1.3E−04	1.6	3.4E−07	1.9	7.6E−07	1.9	3.4E−06	1.4
64	2.6E−06	2.0	6.0E−06	2.1	2.0E−05	2.7	7.3E−08	2.2	1.7E−07	2.2	7.3E−07	2.2
128	7.7E−07	1.8	1.7E−06	1.8	4.8E−06	2.1	1.8E−08	2.0	4.1E−08	2.0	1.9E−07	1.9

Table 6
Convergence rates: case: $C = 1.4 \times 10^{-2}, \mathbf{k} = (1,0), \rho_d/\rho_g = 10^{-3}$.

N_{cells}	L_1	R_1	L_2	R_2	L_∞	R_∞	L_1	R_1	L_2	R_2	L_∞	R_∞
	density-gas						*x-vel-gas*					
16	4.2E−07	–	9.5E−07	–	2.7E−06	–	2.5E−06	–	5.7E−06	–	1.6E−05	–
32	1.1E−07	2.0	2.4E−07	2.0	6.8E−07	2.0	6.4E−07	2.0	1.4E−06	2.0	4.0E−06	2.0
64	2.7E−08	2.0	6.0E−08	2.0	1.7E−07	2.0	1.6E−07	2.0	3.6E−07	2.0	1.0E−06	2.0
128	6.8E−09	2.0	1.5E−08	2.0	4.3E−08	2.0	4.0E−08	2.0	9.0E−08	2.0	2.5E−07	2.0
	density-dust						*x-vel-dust*					
16	2.5E−08	–	5.6E−08	–	1.6E−07	–	1.7E−06	–	3.7E−06	–	1.1E−05	–
32	4.8E−09	2.4	1.1E−08	2.4	3.0E−08	2.4	4.2E−07	2.0	9.3E−07	2.0	2.6E−06	2.0
64	3.6E−10	3.7	8.0E−10	3.7	2.4E−09	3.7	1.1E−07	2.0	2.3E−07	2.0	6.7E−07	2.0
128	3.5E−10	0.1	7.7E−10	0.1	2.2E−09	0.1	2.7E−08	2.0	5.9E−08	2.0	1.7E−07	2.0

Table 7
Convergence rates: case: $D = 1.4 \times 10^{-2}, \mathbf{k} = (1,0), \rho_d/\rho_g = 10^{3}$.

N_{cells}	L_1	R_1	L_2	R_2	L_∞	R_∞	L_1	R_1	L_2	R_2	L_∞	R_∞
	density-gas						*x-vel-gas*					
16	3.1E−07	–	6.9E−07	–	1.9E−06	–	5.5E−06	–	1.2E−05	–	3.4E−05	–
32	7.5E−08	2.0	1.7E−07	2.0	4.7E−07	2.0	1.4E−06	2.0	3.1E−06	2.0	8.7E−06	2.0
64	1.8E−08	2.1	4.0E−08	2.1	1.1E−07	2.1	3.5E−07	2.0	7.8E−07	2.0	2.2E−06	2.0
128	4.1E−09	2.1	9.2E−09	2.1	2.6E−08	2.1	8.8E−08	2.0	1.9E−07	2.0	5.5E−07	2.0
	density-dust						*x-vel-dust*					
16	1.4E−06	–	3.0E−06	–	8.5E−06	–	5.5E−06	–	1.2E−05	–	3.4E−05	–
32	3.3E−07	2.0	7.4E−07	2.0	2.1E−06	2.0	1.4E−06	2.0	3.1E−06	2.0	8.7E−06	2.0
64	7.8E−08	2.1	1.7E−07	2.1	4.9E−07	2.1	3.5E−07	2.0	7.8E−07	2.0	2.2E−06	2.0
128	1.7E−08	2.2	3.8E−08	2.2	1.1E−07	2.2	8.8E−08	2.0	1.9E−07	2.0	5.5E−07	2.0

Table 8
Convergence rates: case: $E = 1.4 \times 10^{-2}, \mathbf{k} = (1,0), \rho_d/\rho_g = 1$.

N_{cells}	L_1	R_1	L_2	R_2	L_∞	R_∞	L_1	R_1	L_2	R_2	L_∞	R_∞
	density-gas						*x-vel-gas*					
16	3.0E−06	–	6.8E−06	–	1.9E−05	–	2.6E−06	–	5.9E−06	–	1.7E−05	–
32	1.5E−06	1.0	3.3E−06	1.0	9.4E−06	1.0	1.1E−06	1.3	2.4E−06	1.3	6.7E−06	1.3
64	7.4E−07	1.0	1.6E−06	1.0	4.6E−06	1.0	4.0E−07	1.4	8.8E−07	1.4	2.5E−06	1.4
128	2.3E−07	1.7	5.1E−07	1.7	1.5E−06	1.7	1.2E−07	1.8	2.6E−07	1.8	7.4E−07	1.8
	density-dust						*x-vel-dust*					
16	3.3E−05	–	7.3E−05	–	2.0E−04	–	2.7E−06	–	6.0E−06	–	1.7E−05	–
32	9.0E−06	1.9	2.0E−05	1.9	5.6E−05	1.9	1.0E−06	1.4	2.3E−06	1.4	6.5E−06	1.4
64	3.0E−06	1.6	6.7E−06	1.6	1.9E−05	1.6	3.6E−07	1.5	8.1E−07	1.5	2.3E−06	1.5
128	8.7E−07	1.8	1.9E−06	1.8	5.5E−06	1.8	1.0E−07	1.8	2.3E−07	1.8	6.6E−07	1.8

would not have been trivially expected. Finally, in the mildly stiff regime, the convergence rate reduces to approximately first order, as shown in Tables 13 dust-to-gas ratio of 1. This is however, not unexpected because in this case accuracy of the two-fluid algorithm also drops.

Table 9
Convergence rates: case: $F = 1.4 \times 10^{-2}, \mathbf{k} = (2,1)/\sqrt{5}, \rho_d/\rho_g = 1$.

N_{cells}	L_1	R_1	L_2	R_2	L_∞	R_∞	L_1	R_1	L_2	R_2	L_∞	R_∞
	density-gas						*x-vel-gas*					
16	2.1E−05	–	2.4E−05	–	3.3E−05	–	5.4E−05	–	6.0E−05	–	8.5E−05	–
32	6.0E−06	1.8	6.6E−06	1.8	9.4E−06	1.8	1.5E−05	1.9	1.6E−05	1.9	2.3E−05	1.9
64	1.6E−06	1.9	1.7E−06	1.9	2.5E−06	1.9	3.8E−06	2.0	4.2E−06	2.0	6.0E−06	2.0
128	4.0E−07	2.0	4.4E−07	2.0	6.3E−07	2.0	9.6E−07	2.0	1.1E−06	2.0	1.5E−06	2.0
	y-vel-gas						*pressure*					
16	1.7E−05	–	1.8E−05	–	2.6E−05	–	3.0E−05	–	3.3E−05	–	4.7E−05	–
32	4.8E−06	1.8	5.4E−06	1.8	7.6E−06	1.8	8.4E−06	1.8	9.3E−06	1.8	1.3E−05	1.8
64	1.3E−06	1.9	1.4E−06	1.9	2.0E−06	1.9	2.2E−06	1.9	2.4E−06	1.9	3.4E−06	1.9
128	3.3E−07	2.0	3.6E−07	2.0	5.1E−07	2.0	5.6E−07	2.0	6.2E−07	2.0	8.8E−07	2.0
	density-dust						*x-vel-dust*					
16	2.3E−04	–	2.5E−04	–	3.6E−04	–	7.8E−05	–	8.6E−05	–	1.2E−04	–
32	4.9E−05	2.2	5.5E−05	2.2	8.0E−05	2.2	2.0E−05	1.9	2.2E−05	1.9	3.2E−05	1.9
64	1.6E−05	1.7	1.7E−05	1.7	2.5E−05	1.7	5.1E−06	2.0	5.7E−06	2.0	8.0E−06	2.0
128	3.8E−06	2.1	4.3E−06	2.0	9.4E−06	1.4	1.3E−06	2.0	1.4E−06	2.0	2.0E−06	2.0
	y-vel-dust											
16	1.3E−04	–	1.5E−04	–	2.1E−04	–						
32	3.5E−05	1.9	3.9E−05	1.9	5.5E−05	1.9						
64	8.8E−06	2.0	9.8E−06	2.0	1.4E−05	2.0						
128	2.2E−06	2.0	2.5E−06	2.0	3.5E−06	2.0						

Table 10
Convergence rates: case: $G = 1.4 \times 10^{-2}, \mathbf{k} = (2,1)/\sqrt{5}, \rho_d/\rho_g = 1$.

N_{cells}	L_1	R_1	L_2	R_2	L_∞	R_∞	L_1	R_1	L_2	R_2	L_∞	R_∞
	density-gas						*x-vel-gas*					
16	5.8E−05	–	6.4E−05	–	9.7E−05	–	5.0E−05	–	5.6E−05	–	8.7E−05	–
32	1.3E−05	2.2	1.5E−05	2.1	2.4E−05	2.0	1.6E−05	1.6	1.8E−05	1.6	2.8E−05	1.6
64	3.7E−06	1.8	4.1E−06	1.9	6.3E−06	1.9	5.3E−06	1.6	6.0E−06	1.6	8.7E−06	1.7
128	1.5E−06	1.3	1.6E−06	1.3	2.6E−06	1.3	2.0E−06	1.4	2.3E−06	1.4	3.5E−06	1.3
	y-vel-gas						*pressure*					
16	2.5E−05	–	3.0E−05	–	7.0E−05	–	8.2E−05	–	9.0E−05	–	1.4E−04	–
32	3.2E−05	−0.4	3.6E−05	−0.2	5.6E−05	0.3	1.8E−05	2.2	2.1E−05	2.1	3.3E−05	2.0
64	2.5E−05	0.4	2.8E−05	0.4	3.9E−05	0.5	5.2E−06	1.8	5.8E−06	1.9	8.8E−06	1.9
128	1.5E−05	0.7	1.6E−05	0.7	2.3E−05	0.8	2.1E−06	1.3	2.3E−06	1.3	3.7E−06	1.3
	density-dust						*x-vel-dust*					
16	9.6E−05	–	1.1E−04	–	2.0E−04	–	4.9E−05	–	5.4E−05	–	8.1E−05	–
32	3.8E−05	1.3	4.4E−05	1.3	7.8E−05	1.3	1.8E−05	1.4	2.0E−05	1.4	2.9E−05	1.5
64	1.7E−05	1.1	1.9E−05	1.2	3.1E−05	1.3	6.1E−06	1.6	6.8E−06	1.6	9.8E−06	1.6
128	8.0E−06	1.1	9.1E−06	1.1	1.5E−05	1.1	2.2E−06	1.4	2.5E−06	1.4	3.8E−06	1.4
	y-vel-dust											
16	1.8E−04	–	2.0E−04	–	2.9E−04	–						
32	8.1E−05	1.2	9.0E−05	1.2	1.3E−04	1.2						
64	3.8E−05	1.1	4.2E−05	1.1	5.9E−05	1.1						
128	1.8E−05	1.1	2.0E−05	1.1	2.8E−05	1.1						

6.3. Streaming instability

In this last section we carry out the test proposed in [28] (hereafter, YJ07), which consists of following the growth of an initial perturbation unstable to the streaming instability [29]. The test setup, while considerably simplified with respect to a Keplerian disk, preserves the key dynamical features leading to the streaming instability in a protoplanetary disk [14,15] and, with the available analytic solution (for the linear regime), provides a clean test for a simulation code. The test consists of simulating an axisymmetric shearing sheet in which dust particles drift with respect to the gas due to the radial pressure gradient affecting the gas but not the dust. Both vertical structure (along the y-direction) and self-gravity are ignored. After neglecting the vertical derivatives (along the y-axis), the governing equations for the gas component in a shearing sheet can be written as in Eq. (1) provided that we replace f_d in the source term in (2) with

$$f_d^\Omega = f_d + \Omega \begin{pmatrix} 2(u_{g,y} + \eta v_k) \\ -\frac{1}{2} u_{g,x} \\ 0 \end{pmatrix}, \tag{107}$$

Table 11
Convergence rates: case: $H = 1.4 \times 10^{-2}, \mathbf{k} = (2,1)/\sqrt{5}, \rho_d/\rho_g = 10^{-3}$.

N_{cells}	L_1	R_1	L_2	R_2	L_∞	R_∞	L_1	R_1	L_2	R_2	L_∞	R_∞
	density-gas						*x-vel-gas*					
16	1.5E−05	–	1.7E−05	–	2.4E−05	–	4.3E−05	–	4.8E−05	–	6.7E−05	–
32	4.5E−06	1.8	5.0E−06	1.8	7.1E−06	1.8	1.2E−05	1.9	1.3E−05	1.9	1.9E−05	1.8
64	1.2E−06	1.9	1.3E−06	1.9	1.9E−06	1.9	3.0E−06	2.0	3.4E−06	2.0	4.8E−06	2.0
128	3.0E−07	2.0	3.3E−07	2.0	4.8E−07	2.0	7.5E−07	2.0	8.4E−07	2.0	1.2E−06	2.0
	y-vel-gas						*pressure*					
16	1.1E−06	–	1.2E−06	–	1.8E−06	–	2.1E−05	–	2.4E−05	–	3.4E−05	–
32	5.4E−07	1.0	6.0E−07	1.1	8.6E−07	1.1	6.3E−06	1.8	7.0E−06	1.8	9.9E−06	1.8
64	2.0E−07	1.4	2.3E−07	1.4	3.3E−07	1.4	1.7E−06	1.9	1.8E−06	1.9	2.6E−06	1.9
128	6.4E−08	1.7	7.1E−08	1.7	1.0E−07	1.7	4.2E−07	2.0	4.7E−07	2.0	6.7E−07	2.0
	density-dust						*x-vel-dust*					
16	4.1E−07	–	4.6E−07	–	6.5E−07	–	1.8E−04	–	2.0E−04	–	2.8E−04	–
32	1.4E−07	1.6	1.5E−07	1.6	2.1E−07	1.6	4.9E−05	1.9	5.4E−05	1.9	7.6E−05	1.9
64	5.2E−08	1.4	5.8E−08	1.4	8.2E−08	1.4	1.2E−05	2.0	1.4E−05	2.0	1.9E−05	2.0
128	2.0E−08	1.4	2.2E−08	1.4	3.4E−08	1.3	3.1E−06	2.0	3.5E−06	2.0	4.9E−06	2.0
	y-vel-dust											
16	3.4E−05	–	3.7E−05	–	5.2E−05	–						
32	9.9E−06	1.8	1.1E−05	1.8	1.6E−05	1.8						
64	2.6E−06	1.9	2.9E−06	1.9	4.1E−06	1.9						
128	6.7E−07	2.0	7.4E−07	2.0	1.0E−06	2.0						

Table 12
Convergence rates: case: $I = 1.4 \times 10^{-2}, \mathbf{k} = (2,1)/\sqrt{5}, \rho_d/\rho_g = 10^{3}$.

N_{cells}	L_1	R_1	L_2	R_2	L_∞	R_∞	L_1	R_1	L_2	R_2	L_∞	R_∞
	density-gas						*x-vel-gas*					
16	6.5E−06	–	7.2E−06	–	1.0E−05	–	1.7E−04	–	1.9E−04	–	2.6E−04	–
32	2.3E−06	1.5	2.5E−06	1.5	3.5E−06	1.5	1.4E−04	0.3	1.6E−04	0.3	2.2E−04	0.2
64	1.0E−06	1.2	1.1E−06	1.2	1.6E−06	1.2	8.9E−05	0.7	9.9E−05	0.7	1.4E−04	0.7
128	5.3E−07	0.9	5.9E−07	0.9	8.3E−07	0.9	5.4E−05	0.7	6.0E−05	0.7	8.4E−05	0.7
	y-vel-gas						*pressure*					
16	2.3E−04	–	2.6E−04	–	3.6E−04	–	9.1E−06	–	1.0E−05	–	1.4E−05	–
32	2.0E−04	0.2	2.2E−04	0.2	3.1E−04	0.2	3.2E−06	1.5	3.5E−06	1.5	5.0E−06	1.5
64	1.2E−04	0.7	1.4E−04	0.7	2.0E−04	0.6	1.4E−06	1.2	1.5E−06	1.2	2.2E−06	1.2
128	7.5E−05	0.7	8.3E−05	0.7	1.2E−04	0.7	7.4E−07	0.9	8.2E−07	0.9	1.2E−06	0.9
	density-dust						*x-vel-dust*					
16	2.2E−05	–	2.4E−05	–	3.3E−05	–	3.8E−04	–	4.1E−04	–	5.8E−04	–
32	9.1E−06	1.2	1.0E−05	1.2	1.4E−05	1.2	2.0E−04	0.9	2.3E−04	0.9	3.2E−04	0.9
64	4.0E−06	1.2	4.4E−06	1.2	6.2E−06	1.2	1.1E−04	0.9	1.2E−04	0.9	1.7E−04	0.9
128	1.9E−06	1.1	2.1E−06	1.1	3.0E−06	1.1	5.8E−05	0.9	6.5E−05	0.9	9.2E−05	0.9
	y-vel-dust											
16	5.2E−04	–	5.8E−04	–	8.1E−04	–						
32	2.9E−04	0.9	3.2E−04	0.9	4.5E−04	0.8						
64	1.5E−04	0.9	1.7E−04	0.9	2.4E−04	0.9						
128	8.2E−05	0.9	9.1E−05	0.9	1.3E−04	0.9						

where Ω is the angular velocity of the shearing sheet, $v_k = \Omega r$ is the azimuthal velocity at radial distance r, and η is a dimensionless parameter expressing the strength of the radial pressure gradient with respect to the centrifugal force. The source term for the dust fluid is modified in an analogous way, except that in this case we set $\eta = 0$. Finally, the particle equations of motion are also modified, namely Eq. (4) now reads

$$\frac{dv_d}{dt} = \omega \cdot v_d - \kappa_d (v_d - u_g), \quad \omega = \begin{pmatrix} 0 & 2 & 0 \\ -\frac{1}{2} & 0 & 0 \\ 0 & 0 & 0 \end{pmatrix}. \tag{108}$$

In principle the y-component of the particles position should also be modified, but this is irrelevant due to the azimuthal symmetry of the system.

In order to perform the test, the gas and dust velocities are initialized to the equilibrium solution given by Nakagawa et al. [22] (or Eq. (7) in YJ05). Gas density and pressure are set according to

Table 13
Convergence rates: case: $L = 1.4 \times 10^{-2}, \mathbf{k} = (2,1)/\sqrt{5}, \rho_d/\rho_g = 1$.

N_{cells}	L_1	R_1	L_2	R_2	L_∞	R_∞	L_1	R_1	L_2	R_2	L_∞	R_∞
	density-gas						*x-vel-gas*					
16	3.2E−05	–	3.5E−05	–	4.9E−05	–	4.3E−05	–	4.8E−05	–	6.7E−05	–
32	8.1E−06	2.0	9.0E−06	2.0	1.3E−05	1.9	4.4E−05	−0.0	4.9E−05	−0.0	6.9E−05	−0.0
64	1.6E−05	−1.0	1.8E−05	−1.0	2.5E−05	−1.0	4.3E−05	0.0	4.8E−05	0.0	6.8E−05	0.0
128	8.8E−06	0.9	9.7E−06	0.9	1.4E−05	0.9	1.9E−05	1.2	2.1E−05	1.2	3.0E−05	1.2
	y-vel-gas						*pressure*					
16	2.6E−05	–	2.9E−05	–	4.1E−05	–	4.4E−05	–	4.9E−05	–	6.9E−05	–
32	8.1E−05	−1.6	9.0E−05	−1.6	1.3E−04	−1.6	1.1E−05	2.0	1.3E−05	2.0	1.8E−05	2.0
64	5.9E−05	0.5	6.6E−05	0.5	9.3E−05	0.5	2.2E−05	−1.0	2.5E−05	−1.0	3.5E−05	−1.0
128	2.4E−05	1.3	2.7E−05	1.3	3.8E−05	1.3	1.2E−05	0.9	1.4E−05	0.9	1.9E−05	0.9
	density-dust						*x-vel-dust*					
16	1.3E−04	–	1.4E−04	–	2.0E−04	–	5.2E−05	–	5.7E−05	–	8.0E−05	–
32	1.6E−04	−0.3	1.7E−04	−0.3	2.5E−04	−0.3	4.1E−05	0.3	4.6E−05	0.3	6.5E−05	0.3
64	1.1E−04	0.6	1.2E−04	0.5	1.7E−04	0.5	4.4E−05	−0.1	4.8E−05	−0.1	6.9E−05	−0.1
128	4.4E−05	1.3	4.9E−05	1.3	7.0E−05	1.3	2.0E−05	1.2	2.2E−05	1.2	3.1E−05	1.2
	y-vel-dust											
16	1.8E−04	–	2.0E−04	–	2.8E−04	–						
32	1.2E−04	0.5	1.4E−04	0.5	1.9E−04	0.5						
64	6.9E−05	0.8	7.7E−05	0.8	1.1E−04	0.8						
128	2.7E−05	1.4	3.0E−05	1.4	4.2E−05	1.4						

Table 14
Run set.

Case	κ_0	**k**	ρ_d/ρ_g	s/Ω
linA	0.357	(30,0,30)	3	0.4190204
linB	0.357	(6,0,6)	0.2	0.0154764

$$\rho_g = 1.4, \quad P = \frac{\rho_g}{\gamma x_p}, \tag{109}$$

where $x_p \equiv \eta v_k/c = 0.05$ as in YJ05, and ρ_d is set according to a specified dust-to-gas ratio (see below). Note that the parameters Ω, r and η need not be specified as long as one expresses time, distances and velocities in units of $\Omega^{-1}, \eta r$, and $\eta\Omega r = \eta v_k$, respectively. Finally, a perturbation unstable to streaming instability, is added to the initial equilibrium values. YJ07 provide two sets of the eigen-modes for the perturbation amplitudes of each variable, corresponding to what they refer to as linA and linB cases. Some basic features of these cases, including the wave vector, the dust-to-gas ratio and the normalized growth rate (s/Ω), are summarized in Table 14, full details are provided in YJ07. The perturbations are in the radial and vertical directions (x, z) but not in the azimuthal direction (y). The system is evolved using an isothermal equation of state. Note that these tests are basically in the non-stiff regime, as $k_{g,d}\Delta t \leqslant 0.1$.

In Fig. 3 we report the simulated growth rate of the instability, for both gas and dust variables, as a function of the resolution expressed in number of cells per perturbation wavelength. The top and bottom panels correspond to case linA and linB, respectively, and open and filled dots refer to the two-fluid and hybrid algorithm, respectively. With respect to the hybrid algorithm, we always employ 16 particles per cell and a TSC interpolation scheme.

As for the linA case, the test indicates that for both the two-fluid and hybrid algorithms, at least 32 cells per wavelength are required in order to capture the instability growth for all variables and convergence to the analytic solution is basically achieved with 64 cells per wavelength. The linB case is much more challenging and now at least 128 cells per wavelength are necessary in order to capture the instability. Note so that because the gas–dust coupling is non-stiff, we do not expect any particular advantage of our scheme with respect to other second order schemes. In fact, our results are comparable to those of Balsara et al. [1], who use an approach based on a second order Godunov's method, and less accurate then those in YJ05, who instead use a sixth order spectral method.

7. Discussion and summary

We have presented a stable and convergent method for studying a system of gas and dust coupled through viscous drag in both non-stiff and stiff regimes.

Our approach consists of updating the fluid quantities using a two-fluid model and then using the updated fluid solution to advance the individual particle solutions with a self-consistent time evolution of the gas velocity in the estimate of the drag force.

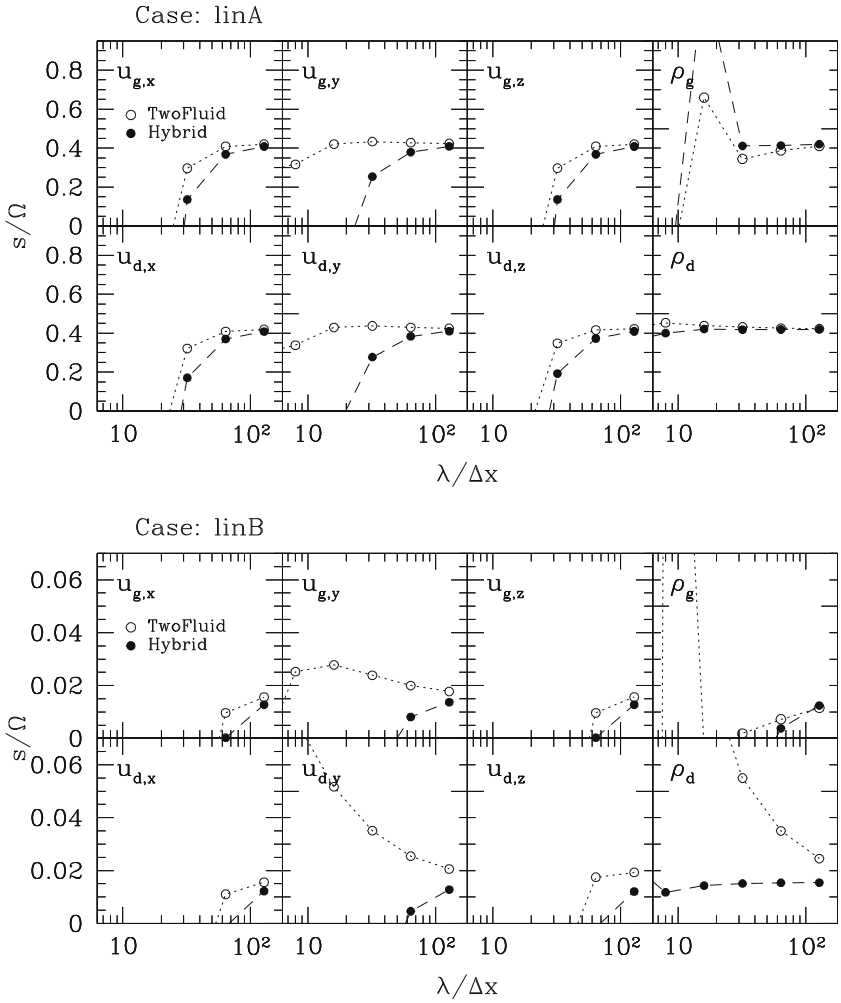

Fig. 3. Growth rate of the simulated streaming instability, for both gas and dust variables, as a function of the number of cells per perturbation wavelength. The top and bottom panels correspond to case linA and linB, respectively, and open and filled dots refer to the two-fluid and hybrid algorithm, respectively.

In our derivation of the two-fluid method, we first obtain a fluid description of the dust component using a particle–mesh method, and then we study the modified gas–dust hyperbolic system following the approach in Miniati and Colella [19]. Based on this analysis we formulate a predictor step providing first order accurate reconstruction of the time-averaged state variables at cell interfaces, whence a second order accurate estimates of the conservative fluxes can be obtained. Finally, for the time-discretization for the source terms we use a single-step, second order accurate scheme derived from the α-QSS method proposed by Mott et al. [21]. This completes the description of our two-fluid method.

The fluid description of the dust component Eqs. (23) and (24) assumes the simplest type of closure which neglects dispersion velocity terms in the momentum equation. However, since the particle distribution is known, different and more suitable closures can be constructed according to the specifics of the aimed application. This is relevant when the dust–gas coupling is stiff and the dust backreaction is important, e.g. high dust density and large dust grain size [13], because in this case the gas tends to follow the dust and the anisotropic particle motions may not be quickly damped.

In order to advance the individual particle solutions we use the fluid solution to determine the time dependence of the gas velocity entering the drag terms. This allows us to derive a particle integration scheme, also based on the α-QSS method, which is second order accurate regardless of the strength of dust–gas coupling.

Remarkably, the particle method that we employ contains no explicit term arising from the stiff coupling of the particle component, in the sense that each particle motion is integrated individually, though it effectively depends on the other particles solutions, and the scheme is essentially explicit in time, as it only involves the particle solution at time $t = n\Delta t$.

Note that when the dust backreaction on the gas is not important (low dust density), the particle scheme presented in Section 2 can be used together with an unmodified Godunov's method for the gas component. Similarly, a simpler scheme

can be obtained in the limit $\kappa_g \to 0$, as the gas description of the semi-implicit two-fluid scheme in Section 3 reduces to an ordinary explicit Godunov's method, while the stiff solver remains unchanged for the dust component.

A set of benchmark problems show that our method is stable and convergent. In particular, the two-fluid approach is second order accurate both in the non-stiff and stiff regimes, and drops to first order in the intermediate regime as expected theoretically [19]. The hybrid scheme, on the other hand, is second order only in the non-stiff regime. Since, as illustrated in the Sections 6.1 and 6.2.1, both the particle scheme and the two-fluid scheme retain their second order accuracy irrespective of the stiffness conditions, the drop in accuracy in the hybrid approach is most likely due to the difficulty of coupling the gas and the dust fully self-consistently in the stiff regimes. At any rate, the scheme remains stable and first order convergent even in the stiff regime.

We have also tested our code against the streaming instability problem presented in YJ05. This is a clean test and a very relevant one for protoplanetary disk applications. However, due to the specifics of the test set up, the gas–dust coupling is non-stiff, so that we do not expect any particular advantage of our scheme with respect to other second order schemes. In fact, our results are comparable to those of Balsara et al. [1], who use an approach based on a second order Godunov's method, and less accurate then those in YJ05, who instead use a sixth order spectral method.

Finally, although the present analysis focuses on the Epstein regime for the functional form of drag force, in principle extension to the case of Stokes regime should also be possible. This would require a modification of both the Godunov predictor step and the semi-implicit scheme in Section 3.2. In addition, the present scheme can also be extended to the case of dust particles of multiple sizes. A complication arises, however, due to the fact that one cannot straightforwardly define a single effective dust component to which the gas is coupled via the drag force. Such complication seems inevitable and of general character, i.e. it is not restricted to the approach presented in this paper, when the coupling is stiff and the dust backreaction is dynamically important. So, for a limited number of dust components of different grain size the present method can be modified by defining an extended system in which each dust component is represented separately. This approach, however, becomes cumbersome and expensive when the number of dust species is large, and a method for constructing a single effective dust component should be investigated in such cases.

Acknowledgment

I acknowledge very useful and encouraging discussions with P. Colella about various algorithmic issues, with L. Fouchet, A. Booley about protoplanetary disks and A. Youdin, A. Johanson and H. Klahr about the streaming instability test. I am thankful to an anonymous referee for useful comments to the manuscript. This work was supported by ETH through a Zwicky Prize Fellowship program.

Appendix A. Derivation of the α-QSS based particle scheme

We use the alpha-QSS method to integrate the following equations, describing the trajectories in phase-space of dust particles,

$$\frac{dx_d}{dt} = v_d, \tag{A.1}$$

$$\frac{dv_d}{dt} = -\kappa_d (v_d - u_g) - \nabla\phi, \tag{A.2}$$

from time $t = t^n$, when $x_d(t) = x^n$, $v_d(t) = v_d^n$, to $t = t^{n+1} = t^n + \Delta t$.

Following Eq. (11) we first integrate Eq. (A.2) assuming $p_0 = \kappa_d^n$ and $q_0 = \kappa_d^n u_g^n - \nabla\phi$, which yields

$$\tilde{v}_d(t) = v_d^n + (u_g^n - v_d^n)(1 - e^{-\kappa_d^n t}) - t\nabla\phi. \tag{A.3}$$

Note that we have modified the gravitational acceleration term because, as discussed in Section 3.2, gravitational acceleration is not attenuated by drag as both gas and dust are equally accelerated by it. We then obtain a first order accurate expression of the particle position by time integration of the above solution,

$$\tilde{x}_d(\Delta t) = x_d^n + \int_t^{t+\Delta t} d\tau\, \tilde{v}_d(\tau) = x_d^n + \Delta t\, v_d^n + \Delta t(u_g^n - v_d^n)\left(1 - \frac{1 - e^{-\kappa_d \Delta t}}{\kappa_d \Delta t}\right) - \frac{\Delta t^2}{2}\nabla\phi, \tag{A.4}$$

which is equivalent to Eq. (17). For the final corrector step we need to estimate the equivalent of q_* and $\bar{p}$ appearing in (12). The expressions for q_* and $\bar{p}$ in Eqs. (13) and (14), respectively, can be obtained by assuming a linear time dependence for these parameters. Instead for the gas velocity (which play the equivalent role of q in our case) we use the *ansatz* in Eq. (18) with

$$\Delta v_g \equiv v_g^{n+1} - v_g^n.$$

On the other hand, for the drag coefficients (which play the equivalent role of p in our case) we use the following averages consistent with the prescription in Eq. (14),

$$\kappa_s = \frac{1}{2}\left[\kappa_s\left(x_d^n\right) + \kappa_s(\tilde{x}_d)\right], \quad s = d, g.$$

Using Eq. (18) and the above expressions for Δv_g and κ_d, κ_g, we can then integrate Eq. (A.2) to obtain a time dependent solution of the dust particle velocity. Its evaluation at time t^{n+1} gives the solution in Eq. (20) and its integration over a time-step Δt gives the solution (19).

References

[1] D.S. Balsara, D.A. Tilley, T. Rettig, S.D. Brittain, Dust settling in magnetorotationally driven turbulent discs – I. Numerical methods and evidence for a vigorous streaming instability, Mon. Not. R. Astron. Soc. 397 (2009) 24–43.
[2] J.A. Barranco, Three-dimensional simulations of Kelvin–Helmholtz instability in settled dust layers in protoplanetary disks, Astrophys. J. 691 (2009) 907–921.
[3] L. Barrière-Fouchet, J.-F. Gonzalez, J.R. Murray, R.J. Humble, S.T. Maddison, Dust distribution in protoplanetary disks. Vertical settling and radial migration, Astr. Astrophys. 443 (2005) 185–194.
[4] J.B. Bell, P. Colella, J.A. Trangestein, Higher order Godunov methods for general systems of hyperbolic conservation laws, J. Comput. Phys. 82 (1989) 362–397.
[5] J. Birn, J.F. Drake, M.A. Shay, B.N. Rogers, R.E. Denton, M. Hesse, M. Kuznetsova, Z.W. Ma, A. Bhattacharjee, A. Otto, P.L. Pritchett, Geospace environmental modeling (GEM) magnetic reconnection challenge, J. Geoph. Res. 106 (2001) 3715–3720.
[6] G.Q. Chen, C. Levermore, T. Liu, Hyperbolic conservation laws with stiff relaxation terms and entropy, Commun. Pure Appl. Math. 47 (1994) 787–830.
[7] P. Colella, Multidimensional upwind methods for hyperbolic conservation laws, J. Comput. Phys. 82 (1989) 64–84.
[8] J.N. Cuzzi, A.R. Dobrovolskis, J.M. Champney, Particle-gas dynamics in the midplane of a protoplanetary nebula, Icarus 106 (1993). 102+.
[9] A. Dutt, L. Greengard, V. Rokhlin, Spectral deferred correction methods for ordinary differential equations, BIT 40 (2000) 241–266.
[10] G.B. Field, Thermal instability, Astrophys. J. 142 (1965) 531.
[11] S. Fromang, R.P. Nelson, Global MHD simulations of stratified and turbulent protoplanetary discs. II. Dust settling, Astr. Astrophys. 496 (2009) 597–608.
[12] E.T. Toro, Riemann Solvers and Numerical Methods for Fluid Dynamics, second ed., Springer, Berlin, 1997.
[13] P. Garaud, L. Barrière-Fouchet, D.N.C. Lin, Individual and average behavior of particles in a protoplanetary nebula, Astrophys. J. 603 (2004) 292–306.
[14] A. Johansen, H. Klahr, T. Henning, Gravoturbulent formation of planetesimals, Astrophys. J. 636 (2006) 1121–1134.
[15] A. Johansen, J.S. Oishi, M.-M.M. Low, H. Klahr, T. Henning, A. Youdin, Rapid planetesimal formation in turbulent circumstellar disks, Nature 448 (2007) 1022–1025.
[16] G. Laibe, J.-F. Gonzalez, L. Fouchet, S.T. Maddison, SPH simulations of grain growth in protoplanetary disks, Astr. Astrophys. 487 (2008) 265–270.
[17] L.D. Landau, E.M. Lifshitz, Fluid Mechanics, Course of Theoretical Physics, second ed., vol. 6, Pergamon Press, Oxford, 1987.
[18] F. Miniati, P. Colella, Block structured adaptive mesh and time refinement for hybrid, hyperbolic + n-body systems, J. Comput. Phys. 227 (2007) 400–430.
[19] F. Miniati, P. Colella, A modified Godunov's scheme for stiff source conservative hydrodynamics, J. Comput. Phys. 224 (2007) 519–538.
[20] J.J. Monaghan, A. Kocharyan, SPH simulation of multi-phase flow, Comput. Phys. Commun. 87 (1995) 225–235.
[21] D.R. Mott, E.S. Oran, B. van Leer, A quasi-steady-state solver for the stiff ordinary differential equations of reaction kinetics, J. Comput. Phys. 164 (2000) 407–428.
[22] Y. Nakagawa, M. Sekiya, C. Hayashi, Settling and growth of dust particles in a laminar phase of a low-mass solar nebula, Icarus 67 (1986) 375–390.
[23] E.S. Oran, J.P. Boris, Numerical Simulation of Reactive Flow, second ed., Cambridge University Press, Cambridge, UK, 2000.
[24] W.K.M. Rice, G. Lodato, J.E. Pringle, P.J. Armitage, I.A. Bonnell, Accelerated planetesimal growth in self-gravitating protoplanetary discs, Mon. Not. R. Astron. Soc. 355 (2004) 543–552.
[25] J. Saltzman, An unsplit 3D upwind method for hyperbolic conservation laws, J. Comput. Phys. 115 (1994) 153–168.
[26] D. Trebotich, G.H. Miller, P. Colella, D.T. Graves, D.F. Martin, P.O. Schwartz, A tightly coupled particle-fluid model for dna-laden flows in complex microscale geometries, in: K.J. Bathe (Ed.), Proceedings of the Third MIT Conference on Computational Fluid and Solid Mechanics, MIT, USA, 2005, pp. 1018–1022.
[27] G.B. Whitham, Linear and Nonlinear Waves, Wiley-Interscience, New York, 1974.
[28] A. Youdin, A. Johansen, Protoplanetary disk turbulence driven by the streaming instability: linear evolution and numerical methods, Astrophys. J. 662 (2007) 613–626.
[29] A.N. Youdin, J. Goodman, Streaming instabilities in protoplanetary disks, Astrophys. J. 620 (2005) 459–469.